Numerical and Experimental Study on Non-destructive Measuring Method of Axial Load and Natural Frequency of Rails

Yulu Sun

Supervised by

Dr Yusuke Mochida

THE UNIVERSITY OF
WAIKATO
Te Whare Wānanga o Waikato

A thesis submitted in fulfilment of the requirements for the degree of Master of Engineering,

The University of Waikato, 2020.

Abstract

The purpose of this study is to investigate a simple, non-destructive method for monitoring the natural frequencies of the railway tracks subjected to the axial loads. In this study, two kinds of methods are used to obtain the relationship of the axial loads and the natural frequencies. One is the numerical method, and another one is the laboratory experimental method. For the numerical studies, two different numerical analysis methods are used, namely the Finite Element Method (FEM) analysis, and the Rayleigh-Ritz method analysis. The laboratory method has two different equipment to collect signals, one is an accelerometer and the other is a microphone sensor. They both are processed by using the dynamic analysis instrument.

In order to simply and comprehensively verify the practicality, we consider three simply supported beams, which can be considered as a simplified model of the railway track, with different materials and cross-sections. Through the numerical studies, the critical loads and the natural frequencies of the beams are calculated by using the two methods. The results obtained by using the finite element method show a good agreement with the results obtained by the Rayleigh-Ritz method. Through the experiments, it is proved that the laboratory methods can be used to find the natural frequencies of the beams subjected to the axial loads.

The methods used in this study could be put into practical use to simulate and detect the axial load and natural frequency of the railway tracks. With further research, the methods would contribute to development of non-destructive testing methods for the railway tracks.

Acknowledgment

The author would like to express much gratitude to the people who had given so much contribution to the completion of this thesis. The author would like to give thanks specifically for:

Dr. Yusuke Mochida as the main supervisor who had given a lot of guidance, direction, and advice for the research.

Author’s parents who have supported the author to finish the program without any hindrances.

Table content

List of Figures

List of Tables

List of Symbols

E: Young's modulus

ρ: Density

A: Area of cross-section

I: Moment of inertia

A: Coefficient of thermal expansion

P_{cr}: Critical load of structural buckling

P_Q : Applying load

λ_i : Eigenvalue of buckling

$[K_L]$: Total elastic stiffness matrix of the structure

$[K_\sigma]$: Initial stress stiffness matrix of the structure

$\{\delta\}$: Eigen displacement vector

K^*: Geometric stiffness matrix

K: Elastic stiffness matrix

P: Axial load

K_i: Generalized stiffness terms

M_i: Generalized mass terms.

[K]: Coefficient of the matrices

[M]: Coefficient of the matrices

α : Percentage of critical load.

ω : Angular frequency

FRF: Frequency Response Function

FEM: Finite Element Method

FBG: Fiber Bragg Grating

CWR: Continuously Welded Rail

UOW: University of Waikato

Chapter 1. Introduction

1.1 Background Research

Continuously welded rail (CWR) is an important symbol of railway track modernization. Due to its advantages of high operational stability, long rail life, reduced noise and vibration, low maintenance load, and low energy consumption, it has been widely developed worldwide [1, 2]. With the development of the railway transportation industry, people pay more and more attention to how to detect and maintain railways promptly [3, 4]. When high-speed trains pass on railway tracks, it will generate repeated dynamic loads on the tracks. Meanwhile, thermal expansions and contractions also occur due to temperature changes. As the temperature decreases, the tensile stress will cause the rail to break, and when the temperature increases, the compressive stress will cause the rail to buckle. Changes in temperature, and when the train passes on the rail with different acceleration and braking force, some axial force would be induced. All these factors can lead to failure and buckling of tracks [5-7], which are the main causes of trains delay and severe mainline derailment. Rail buckling (Fig.1.1) is one of the main causes of serious train crashes. In the United States, there were 44 accidents caused by rail buckling in 2001. In January 2003, a rail buckling caused a train crash near Sydney, Australia, in which nine people died [8-10]. Therefore, monitoring the axial force of the railway track is particularly necessary.

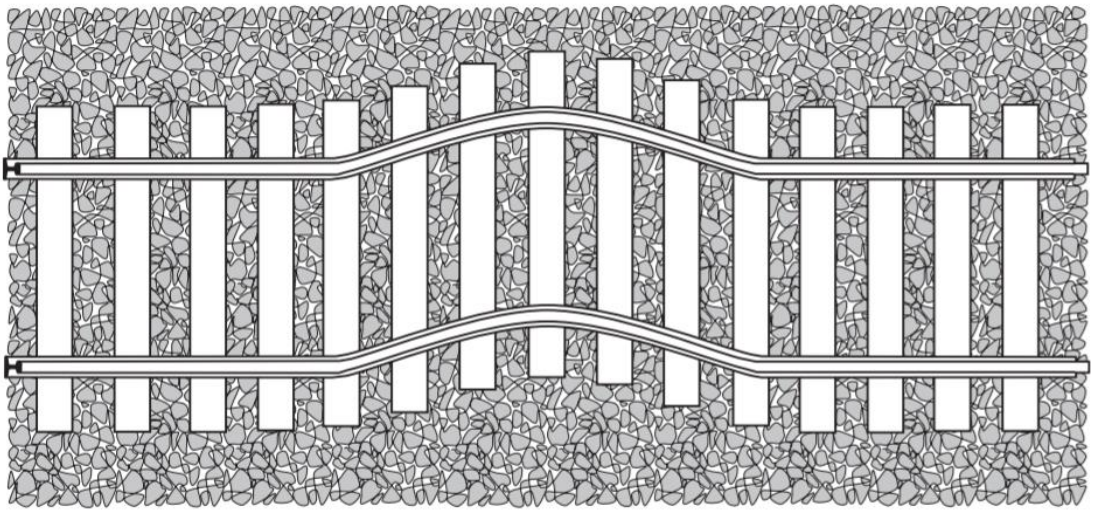

Figure.1.1. The schematic diagram of rail buckling [5].

There are already some experimental methods to measure axial force through vibration. One method is based on the known sensitivity of bending vibrations to the longitudinal stresses involved and excites the track with an electromagnetic shaker at a specified frequency [11]. Then use a laser vibrometer to scan the dynamic displacement along the rail to determine the wavelength of the rail vibration. Combining wavelength with the rail rigidity can be used to determine longitudinal loads. Some researchers use the specific relationship between the acoustic elastic effect of ultrasound and stress for testing [12, 13]. In addition to these laboratory experimental methods, there are many methods based on the numerical study. The numerical experiments often use some finite element analysis software, such as ANSYS [14-16]. Some numerical methods are based on some algorithms. With the algorithms, the problems can be solved using MATLAB [17-19]. Two common algorithms are Fourier Series [19-21] and the Rayleigh-Ritz Method [22, 23].

To detect the residual stress distribution and to decide the inspection period and maintenance cycle of the railway, Takahashi et al. conducted some experiments using two

methods [24]. The first method of detecting stress is to cut the block into small pieces, and pre-install the strain gauge on the small piece, and calculate the residual stress by the released strain. The second is the non-destructive method, which uses X-rays or neutrons to measure the lattice spacing variation of the material structure. The two values have excellent consistency. However, this analysis cannot accurately evaluate the internal stress because it is a technique for balancing only the surface stress.

There is a kind of detection method that is similar to strain gauge measurement. Many researchers have made deep studies in testing the longitudinal force of rails with Fiber Bragg Grating (FBG) sensors. Wang et al. present a method to test longitudinal temperature force by using FBG strain gauges [25]. Yoon et al., with the Brillouin optical correlation domain analysis, tested the longitudinal strain of rails under a certain vertical dynamic load. The testing accuracy can reach up to $\pm 15\mu\varepsilon$ [26]. The advantage of the FBG sensor is that it can measure uniform temperature in addition to mere strain. In addition, it is characterized by longer durability than the strain gauge sensor. If the sensor is installed on the rail prior to the installation of the CWR, it can continuously measure the deformation as long as the sensor works. Theoretically, this can be achieved by using strain gauges only, however durability is important here [12].

The University of Nebraska-Lincoln (UNL) is committed to using ultrasound to monitor longitudinal rail stress, with the support of the Federal Railroad Administration (FRA) [27]. This is a kind of nondestructive method. The aim of their research is therefore to provide the ability of the railway industry to monitor the LRS in an ideal position so that preventive maintenance can be carried out in a reasonable and efficient manner.

They conducted the experiments using the device as shown in Figure 1.2 [27]. The longitudinal source transducer excites an elastic energy pulse that propagates through the coupling wedge with the optimal wedge angle to the solid, allowing the underground longitudinal wave to receive the maximum amount of energy and propagate along the orbit until it is detected by the receiving transducer. The signal received by the transducer is digitized and the signal processing algorithm is used to determine the wave propagation time and wave speed.

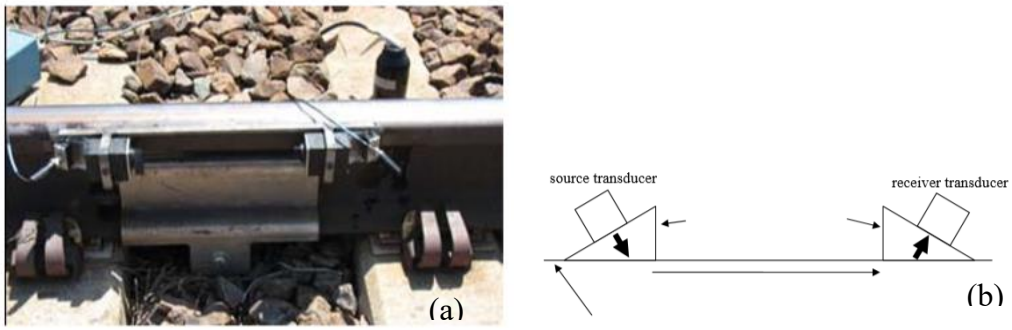

Figure 1.2. (a) Magnetically attached ultrasonic wave speed measurement device. (b) Diagram of the ultrasonic wave speed measurement [27].

The experiments showed the linear relationship between stress and wave velocity and the relationship between ultrasonic velocity and rail stress as shown in Figure 1.3 (a) and (b) respectively. This means that the method of ultrasonically monitoring the longitudinal rail stress is achievable on the rails being used.

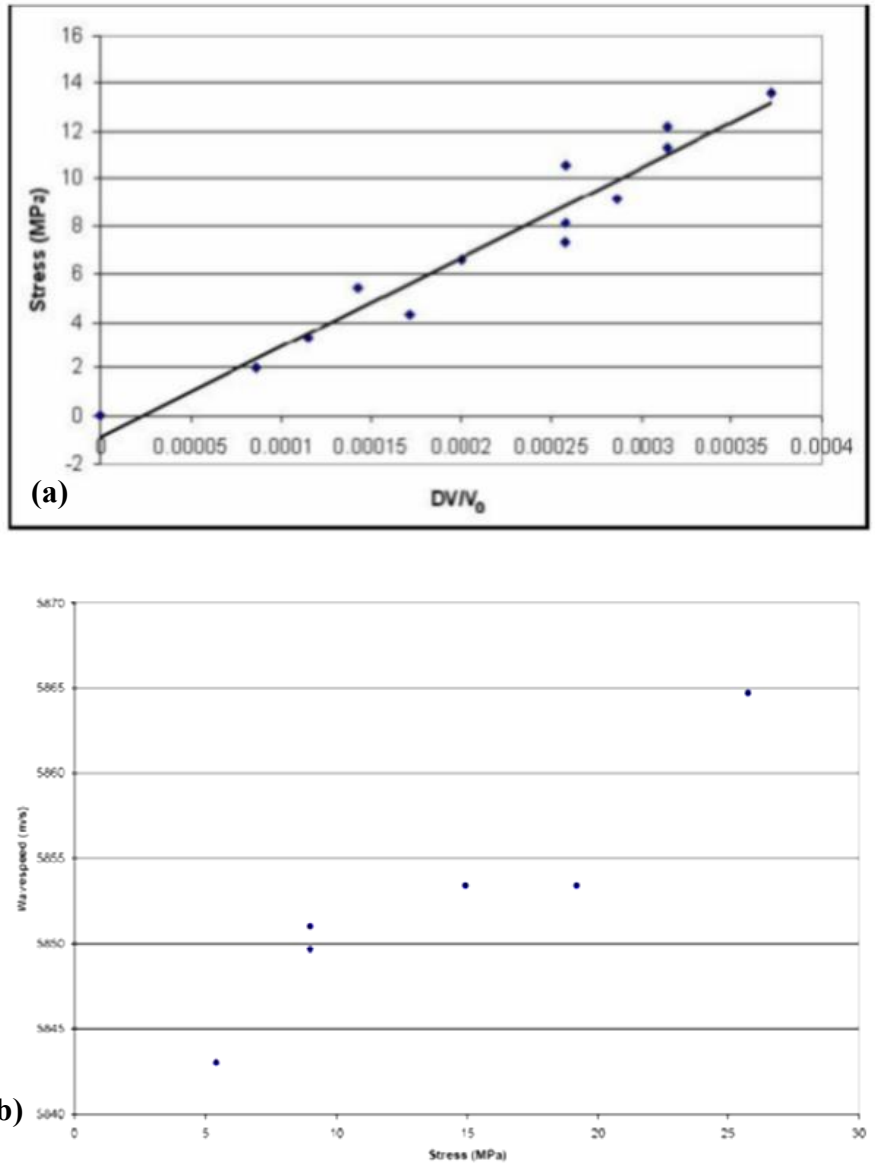

Figure 1.3. The linear relationship (a) between stress and wave velocity and the relationship (b) between ultrasonic velocity and rail stress [27].

However, this method is still very challenging, because the acoustic constant of steel is weak, the competitive influence of material texture, and the acoustic elastic effect are only sensitive to the acousticized area. Permanently installed strain gauges are used in some places but require a reference state and cannot correct plastic creep [11].

The measurement of railway thermal stress is very important for railway safety and track maintenance management. Track stress can be measured by rail uplift or using strain gages, but both have significant limitations. In order to solve the problem of inaccurate current measurement technology, a new technique for measuring contained rail force using rail vibration and laser vibrometry is discussed [28]. This method is based on the known sensitivity of bending vibrations to the longitudinal stresses involved and excites the track with an electromagnetic shaker at a specified frequency. Then use a laser vibrometer to scan the dynamic displacement along the rail to determine the wavelength of the rail vibration. Combining wavelength with rail rigidity can be used to determine longitudinal loads. Although the longitudinal load can be tested by this method, it is limited to some unworn and low-frequency rails. Target accuracy cannot be achieved for worn rails.

In the current research, most existing detection methods are not convenient and effective in practical applications. Most of these usually have some problems like high cost, rail contact, or complex algorithms. For example, the rail uplifting method [29] is very time-consuming and laborious and will affect the daily use of the railway. For the maintenance of the currently completed railway track, the magnitude of the axial force is estimated indirectly based on the total displacement of the track, which is measured using piles installed at predetermined intervals as a reference point [30]. But with this method, the accuracy of the axial force estimation cannot be guaranteed. Therefore, measuring the axial force of railway tracks by the non-destructive way with acceptable accuracy is preferable.

1.2 Objectives

A possibility of a faster, more reliable, and cost-effective method of measuring railway stress using the natural frequency will be investigated. This would improve the safety and efficiency of railway operations. This demand will exist for a long time, and with the increase of axial loads and train speed, the demand is increasing.

The purpose of this study is to investigate a simple, non-destructive method for detecting axial force in the railway track using its natural frequencies.

Chapter 2. Background Theory

Numerical studies were performed to model the behavior of the railway track under the compressive axial loading, which would happen during non-contact monitoring of rails. Two different analysis methods will be used in the study, one is the Finite Element Method (FEM) analysis, and the other is the Rayleigh-Ritz method analysis.

2.1 The Finite Element Method Analysis

With the rapid development of science and technology, the finite element analysis has become more and more popular and is widely used in various engineering fields. Therefore, it should be able to easily calculate the mechanical problems of railway track structures. In this research, the finite element analysis software ANSYS is used to study the mechanical problems of the track structure. ANSYS is currently the most widely used and most powerful finite element analysis software. After 40 years of development, a large-scale general-purpose finite element analysis software integrating structure, fluid, electric field, magnetic field, acoustic field, and thermal analysis has been formed. In order to obtain the analysis results of the axial force and natural frequencies of rails, it is necessary to perform an eigenvalue buckling analysis and a modal analysis in ANSYS [31].

The main purpose of this section is to calculate the deformation and the natural frequencies of a rail under the influence of axial force. The traditional railway track is composed of mainly five parts: steel rail, under-rail rubber pad, sleeper, trackbed, and foundation bed.

In this research, however, we use simply supported beams, which is considered an effectual model of a segment the CWR between the sleepers. The geometric dimensions of the rails

are modeled according to the actual dimensions of the beam used in the experimental tests later, and solid elements are selected for discrete processing.

2.1.1 Geometry

For the eigenvalue buckling and modal analysis of the structure, the first step is to model the rail as a beam in the geometry module, which is called SpaceClaim in ANSYS. After the coordinate system is selected, the surface is generated according to the cross-section of the beam, and then the surface is pulled into a body. The complete I beam model is shown in Figure 2.1.

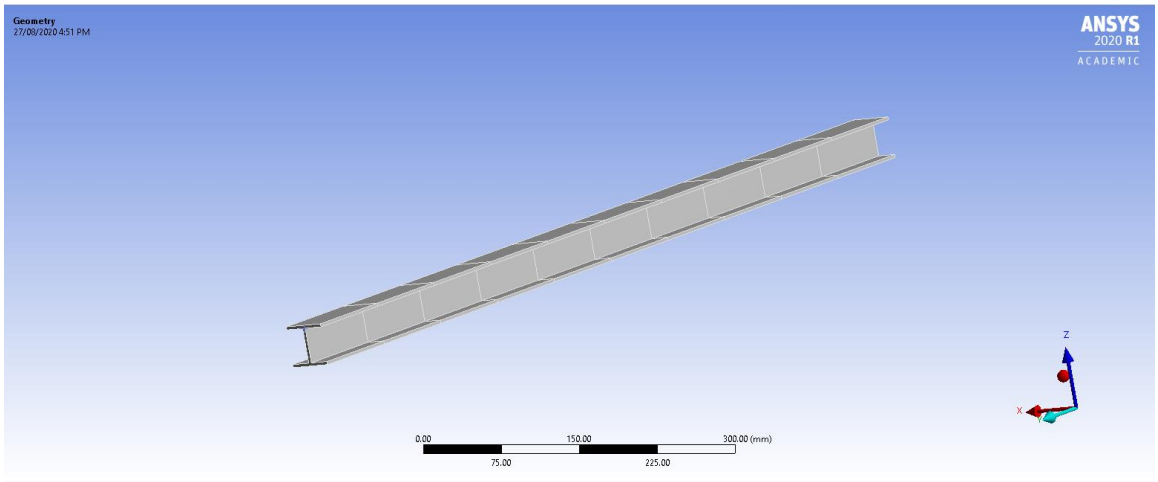

Figure 2.1. Schematic of I beam built with ANSYS.

2.1.2 Meshing

After the geometry is completed, the model needs to be meshed. we meshed the model with the element sizes of 10mm.

2.1.3 Static Structural Analysis

The next step is the static structural analysis. First of all, apply remoted displacements on the surfaces of both ends and apply a force on the model, then solve for the equivalent stress, total deformation, and normal stress. The normal stress multiplied by the cross-sectional area gives the axial force induced.

2.1.4 Eigenvalue Buckling Analysis

Eigenvalue buckling analysis can be done using a built-in module in ANSYS but some deviations for general buckling analysis are briefly given here. When analyzing structural stability, in the analysis of eigenvalue buckling response based on linear elasticity, the critical load of structural buckling can be expressed as [32]:

$$P_{cr_i} = \lambda_i * P_Q \tag{2.1}$$

P_Q is the applying load, λ_i is the eigenvalue of buckling. The function of λ_i is:

$$([\mathrm{K_L}] + \lambda_\mathrm{i}[\mathrm{K}_\sigma]) * \{\delta\} = 0 \tag{2.2}$$

$[K_L]$ is the total elastic stiffness matrix of the structure, $[K_\sigma]$ is the initial stress stiffness matrix of the structure, and $\{\delta\}$ is the eigen displacement vector. The essence of linear buckling finite element calculation is to calculate the minimum critical load of buckling after adding the initial stress stiffness to the overall structure.

After solving the eigenvalues of the model, ANSYS generates the results of the buckling related solution, including buckling eigenvalues, buckling mode shapes, and relative stress distributions. Multiplying the obtained eigenvalues by the applied axial load gives the critical loads for the buckling of the structure.

2.1.5 Modal Analysis

On the basis of static structure analysis, the model can be solved to obtain the natural frequencies, mode shapes, and displacement distribution for the axially loaded beam.

2.2 The Rayleigh-Ritz Method Analysis

For most engineering problems, it is often inconvenient to develop an exact solution. For such problems, it is convenient to use the Rayleigh-Ritz method to obtain eigenvalues and eigenvectors, for example natural frequencies and modal shapes of single-span beam structures under arbitrary boundary conditions. This method has the characteristics of a fast solution and high accuracy.

In the use of the Rayleigh-Ritz method, one of the conditions that we must satisfy is selecting the admissible displacement functions so that they do not violate any geometric constraints and represent the displacement form of the system without any discontinuities. The Rayleigh-Ritz method for vibration problems is based on the principle of that the maximum total potential energy related to vibration is equal to the maximum kinetic energy related to vibration [33].

The linear combination of the natural modes of the system can be represented by an admissible function that does not violate any geometric constraints of the system. The displacement function f is expressed as the sum of a series of the product of unknown weighting coefficients G and the admissible function.

$$f = \sum_i G_i \phi_i \tag{2.3}$$

The potential and kinetic energy terms are expressed as:

$$V_m = \sum_i K_i G_i$$

$$T_m = \omega^2 \sum_i M_i G_i$$

Where K_i and M_i are the generalized stiffness and mass terms.

When $T_m = V_m$ is satisfied, the formula for frequency is obtained.

$$\omega^2 = \frac{\sum_i K_i G_i^2}{\sum_i M_i G_i^2} \tag{2.4}$$

If the displacement *f* is assumed to be exact for the *i*-th natural mode, the equation will be called the *i*-th natural frequency.

$$\omega_i^2 = \frac{K_i}{M_i}$$

According to the Rayleigh principle, the calculated frequency is the upper limit of the fundamental natural frequency. When the expression of the natural frequency with regard to the weighting coefficient is minimized, a typical eigenvalue matrix equation can be obtained.

Let $T_m = \omega^2 \psi_m$

Where ψ_m is a kinetic function.

Known $T_m = V_m$

$$\omega^2 = \frac{V_m}{\psi_m}$$

According to Rayleigh's principle, ω^2 is the upper bound of ω_1^2.

Differentiating this equation with respect to the unknown coefficient *G*,

$$\frac{\partial \omega^2}{\partial G_i} = \frac{(\partial V_m / \partial G_i) - \omega^2 (\partial \psi_m / \partial G_i)}{\psi_m} \tag{2.5}$$

Since ψ_m is finite,

$$\frac{\partial V_m}{\partial G_i} - \omega^2 \frac{\partial \psi_m}{\partial G_i} = 0 \tag{2.6}$$

When there are multiple terms in *f*, a set of equations will be obtained, and each equation is a linear function about G_i. Thus, the equation can be expressed in the form of a matrix.

$$[K]\{G\} - \omega^2 [M]\{G\} = \{0\} \tag{2.7}$$

[K] is the stiffness matrix and [M] is the mass matrix.

The rail system can be simplified and modelled as follows. The railway track is composed of sleepers and tracks. Regarding the two sleepers and the track between them as a unit, the geometric condition of this unit is similar to that of the simply supported beam. A simplified beam model of the rail is shown in Figure 2.2. Simple supports are provided at both ends of the beam. The length of the beam is *L* and *P* is the axial load applied to the beam.

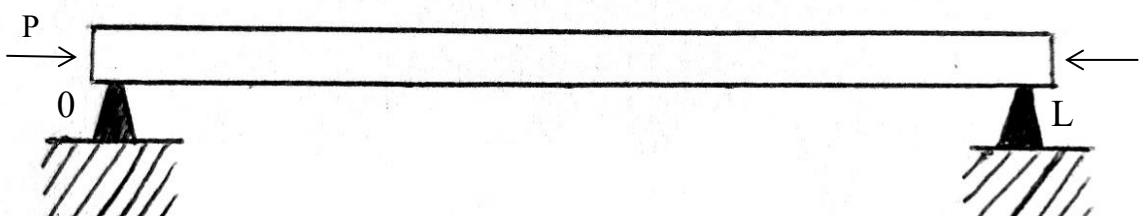

Figure 2.2. The hypothetical beam model.

For this rail model, the geometric constraints are:

At x=0 ϕ=0

At x=L ϕ=0

Admissible function is given by:

$$\phi（x) = \sin(i\pi x / L) \quad \text{for i=1,2,3,4...} \tag{2.8}$$

Then the eigenvalue equation is of this form:

$$[K]\{G\} - P[K^*]\{G\} - \omega^2[M]\{G\} = \{0\} \tag{2.9}$$

If P is buckling load, ω would be zero.

$$[K]\{G\} - P[K^*]\{G\} = \{0\} \tag{2.10}$$

K is the elastic stiffness matrix, and K^* is the geometric stiffness matrix [33].

According to Table 6.1 in the book "*The Rayleigh-Ritz Method for Structure Analysis*" [34].

$$K_{i,j} = \int_0^L EI\,\phi_i''\phi_j''\,dx$$

$$K_{i,j}' = -\int_0^L P\,\phi_i'\phi_j'\,dx$$

and

$$K_{i.j}' = \text{-}P\,K_{i,j}^*$$

$$K_{i,j}^* = \int_0^L \phi_i'\phi_j'\,dx$$

Substituting the admissible function is $\phi（x) = \sin(i\pi x / L)$ into the above equations gives

$$K_{i,j} = \int_0^L EI\,\phi_i^{''}\phi_j^{''}\,dx \;= \int_0^L EI\,(\frac{i\pi}{L})^2(\frac{j\pi}{L})^2 \sin(\frac{i\pi x}{L})\sin(\frac{j\pi x}{L})dx \qquad (2.11)$$

$$K_{i,j}^{*} = \int_0^L \phi_i^{'}\phi_j^{'}\,dx = \int_0^L \left(\frac{i\pi}{L}\right)\left(\frac{j\pi}{L}\right)\cos\left(\frac{i\pi x}{L}\right)\cos\left(\frac{i\pi x}{L}\right)dx \qquad (2.12)$$

When $i = j$,

$$K_{i,j} = EI\,\frac{(i\pi)^4}{2L^3}$$

$$K_{i,j}^{*} = \frac{(i\pi)^2}{2L}$$

When $i \neq j$,

$$K_{i,j} = 0$$

$$K_{i,j}^{*} = 0$$

Convert the derived formula about $K_{i,j}$ and $K_{i,j}^{*}$ into code and input it into MATLAB to get the critical load *P*.

For $i = j$, the equations of $K_{i,j}$ and $K_{i,j}^{*}$ are substituted into the Eq.2.10, then the equation can be written as,

$$\frac{EI}{2L^3}(i\pi^4)[I]\{G\} - \frac{P}{2L}(i\pi^2)[I]\{G\} = \{0\}$$

$$(i\pi^2)[I]\{G\} - \lambda^2[I]\{G\} = \{0\} \quad (i = 1,2,3\cdots)$$

where

$$\lambda^2 = \frac{PL^2}{EI}$$

From the equation above, the *i*-th buckling load can be calculated. Using the column effective length factor according to the Euler's critical load [35-38], *P* is given by

$$P_i = \frac{EI}{(K_{beam}L)^2}(i\pi)^2 \tag{2.13}$$

P_i is *i*-th critical load, *E* is young's modulus, *I* is the second moment of area at the neutral axis, *L* is the unsupported length of the beam. The value of K_{beam} depends on the support conditions at both ends of the beam.

For simply supported beam, K_{beam}=1. In order to get the critical load, convert the formula as follows:

$$P = \frac{EI}{L^2}(i\pi)^2 \tag{2.14}$$

When the load applied is prescribed, the natural frequency ω of the rail can be calculated from the value of the load. If the load is equal to αP , the equation becomes as follows:

$$[K - \alpha P K^*]\{G\} - \omega^2[M]\{G\} = \{0\} \tag{2.15}$$

P is the critical load of the beam, and α is the percentage of critical load.

The equations for the coefficients of the matrix [M] can be found as follows:

$$M_{i,j} = \int_0^L \rho A \phi_i \phi_j dx$$

$$= \rho A \int_0^L \sin\left(\frac{i\pi x}{L}\right)\sin\left(\frac{j\pi x}{L}\right)dx$$

When i≠j,

$$M_{i,j} = 0.$$

When i=j,

$$M_{i,j} = \rho A(\mathrm{L}/2).$$

Based on the results of previous calculations, when *i*=*j*,

$$K_{i,j} = EI\frac{(i\pi)^4}{2L^3} = EI\left(\frac{i\pi}{L}\right)^4 (L/2) \tag{2.16}$$

$$K^*_{i,j} = \frac{(i\pi)^2}{2L} = \left(\frac{i\pi}{L}\right)^2 (L/2) \tag{3.17}$$

Bring the above coefficient $M_{i.j}$, $K_{i,j}$ and $K^*_{i,j}$ into the following eigenvalue equation,

$$[K_{i,j} - \alpha P K^*_{i,j}]\{G\} - \omega^2[M]\{G\} = 0 \tag{2.18}$$

Therefore, the *i*-th line equation of the eigenvalue equation is as follows:

$$\{EI\left(\frac{i\pi}{L}\right)^4 (L/2) - \alpha P\left(\frac{i\pi}{L}\right)^2 (L/2) - \omega^2 \rho A(L/2)\}G_i = 0 \tag{2.19}$$

Put $P = \frac{EI}{L^2}(i\pi)^2$ into Eq.2.19

Simplified to get,

$$\{(1-\alpha)(i\pi)^4 \frac{EI}{L^4} - \omega^2 \rho A\} = 0$$

$$\omega = \sqrt{(1-\alpha)\frac{(i\pi)^4 EI}{\rho A L^4}} \tag{2.20}$$

Since ω is the angular frequency, if the natural frequency f needs to be expressed in Hz, the following calculation is required:

$$f = \frac{\omega}{2\pi} \tag{2.21}$$

Chapter 3. Laboratory Experiment

In order to test the vibration frequency and axial force of the rail, some simple experiments are carried out at the University of Waikato (UOW). The rig used in the experiment consists of three beams used to simulate a railroad track, a clamp used to apply axial pressure to the beams, a strain gauge, and a dynamic test analyzer. In this simulation test, three one-meter beams with different cross-section shapes are used, which are I-beam, rectangular beam, and T-beam. The sizes of the cross-section are shown in Figure 3.1. Three strain gauges are installed on one side of the beams in order to measure the axial force.

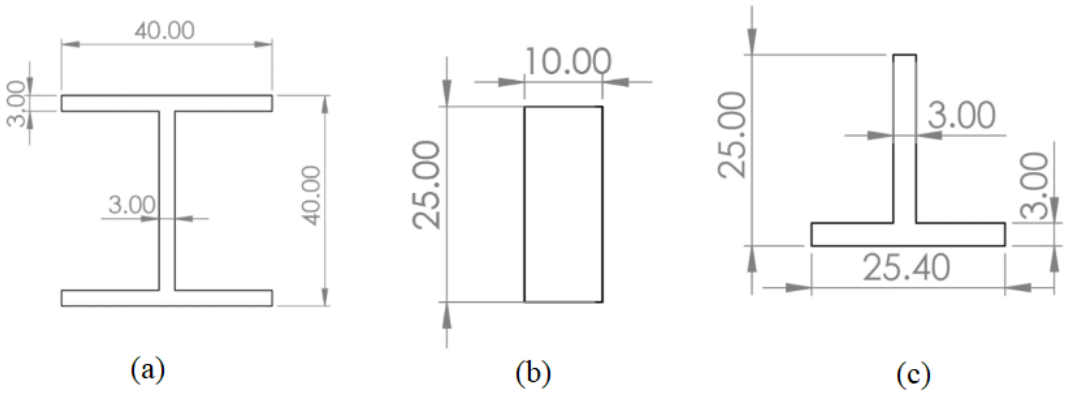

Figure 3.1. The cross-section of (a) I beam, (b) Rectangular beam, and (c) T beam (the dimensions are given in mm).

Table 3.1. Parameters of beams.

	E/(Pa)	Iz/(m^4)	Iy/(m^4)	M/(kg/m)	Area/(m^2)
I beam	6.95E+10	9.21E-08	3.21E-08	9.23E-01	0.000342
T beam	6.95E+10	8.25E-09	4.15E-09	3.83E-01	0.000142
Rectangular beam	2.05E+11	1.30E-08	2.08E-09	1.96E+00	0.00025

Put the assembled model into the clamp made by the UOW workshop. The left end of the clamp is a bottle jack developed by Powerbuilt, which applies axial force to these beams. Before applying pressure to beams, the strain gauges need to be connected with the strain indicator and recorder (Fig.3.2a) developed by Vishay Micro-Measurements. Another instrument used is the CoCo-80 (Fig.3.2b), a handle data logger, dynamic signal analyzer, and vibration collector developed for Crystal Instruments. The input is generated by an impact hammer developed by Brüel & Kjær, and connected with Channel 1. The output is sensed by a triaxial accelerometer developed by PCB Piezotronics. The complete experimental setup is shown in Figure 3.2c.

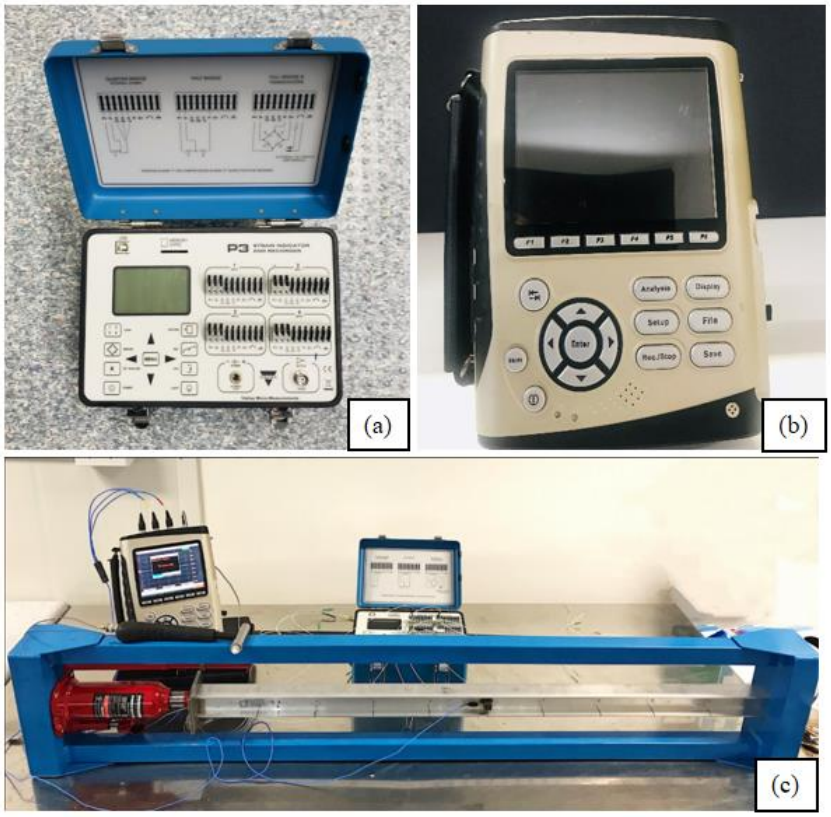

Figure 3.2. Schematic diagram of the experimental device. (a) Strain indicator and recorder (b) The CoCo-80 and (c) Complete experimental model.

After all devices are connected, select the Frequency Response Function (FRF) mode in the CoCo-80 to record. The trigger mode selects Manual-Arm Trigger, and the frequency range is set to a maximum of 360Hz. Each beam is tested under three different pressures. Under each pressure, the output accelerations are measured at three positions of the beam separately. The accelerometer is placed on the left end, center, and right end of the beam. The specific location is shown in Figure 3.3. The distance to the position 1 is 10cm from the left end, the distance to the position 2 is 50cm to the left end, and the distance to the position 3 is 90cm to the left end. And in each testing, there positions of the beam are excited using the impact hammer from left to right.

Figure 3.3. Schematic diagram of the accelerometer installation location.

Chapter 4. Results and Discussions

The critical buckling load and natural frequencies of the beams are calculated by using the Rayleigh-Ritz method and the Finite Element Method (FEM). The results of the Rayleigh-Ritz method are obtained by using MATLAB, and the results of the Finite Element Method are solved by using ANSYS. The natural frequencies of the beam can be captured by using the CoCo-80. There are some differences in the results obtained by different methods. In this chapter, the results obtained by three different methods will be compared for each beam.

4.1. I beam

4.1.1 The Rayleigh-Ritz Method Analysis

With the Rayleigh-Ritz method mentioned in the Chapter 2, the result can be obtained by converting the algorithm into code and inputting it into MATLAB for calculation. Refer to the parameters in Table 4.1 the properties of the I beam are given as $E = 6.95\times10^{10}$ Pa, $I_y = 3.21\times10^{-8}\ m^4$, $I_z = 9.21\times10^{-8}\ m^4$, M = 0.923 Kg/m and $A = 3.42\times10^{-4}\,\mathrm{m}^2$. I_z is the second moment of area for vertical direction and I_y is the second moment of area for horizontal direction. The theoretical results of critical load and natural frequencies for the simply supported beam are shown in Table 4.1 and Table 4.2. The lowest natural frequency of 77.209 Hz is obtained when $I_y = 3.21\times10^{-8}$.

Table 4.1. The theoretical critical load of the I beam.

Buckling load(N)		
	P(Iz)	**P(Iy)**
K=1	63175	22019

Table 4.2. The theoretical natural frequencies of the I beam.

Frequency(Hz)		
Mode	***f*(Iz)**	***f*(Iy)**
1	130.71	77.209
2	523.12	308.83
3	1177.3	694.88

To find a relationship between frequency changes and axial loads, the 20%, 40%, and 60% of critical buckling load were included into MATLAB for calculation, and the natural frequencies are obtained. They are shown in Table 4.3.

Table 4.3. The natural frequency of the I-beam with the axial load *P* (N) obtained using MATLAB (Hz).

Mode \ P	4400	8800.8	13201.2
1	69.065	59.821	48.859
2	126.17	121.35	116.34
3	301.02	293.01	284.75
4	518.66	514.05	509.39
5	687.12	679.27	671.33
6	1172.7	1168.1	1163.5
7	1227.6	1219.8	1212.1
8	2088.4	2083.8	2079.2

4.1.2 The Finite Element Method Analysis

Before performing finite element analysis on the I beam, it is necessary to verify whether the model is established correctly. To build a simply supported beam, two remote displacements are added on the surfaces at both ends. Thereafter, the normal stress and the eigenvalue of buckling can be solved. The number of elements used for the analysis is 1400. Normal force is 455.07N and the first mode eigenvalue is 41.753. According to Eq.2.1, the critical buckling load is 19000.34N, and the natural frequency of the first mode is 77.647Hz. These values agree well with the values given by the Rayleigh-Ritz method.

Subsequently, loads are applied on the surfaces at both ends. The values of loads are 4400N, 8800N, and 13201N. The model can be solved to obtain the natural frequencies and mode

shapes. The 1st to 10th modes of frequency are shown in Table 4.4. Figures 4.1 – 4.3 show the vibration shape under the axial load of 4400N, 8800N, and 13201N respectively. When the applied load is 4400N, the I beam vibrates along the horizontal direction in the 1st, 4th, 7th, and 10th mode. And in 2nd, 6th and 9th modes, the beam vibrates in the vertical direction. Obvious twists can be observed in the other modes. When the applied load is 8800N and 13201N, all of the mode shapes are the same as that of 4400N.

Table 4.4. The natural frequency of the I-beam with the axial load obtained using ANSYS (Hz).

P (N) / Mode	0	4400	8800	13201
1	77.647	68.804	59.341	47.674
2	166.59	123.65	118.92	113.98
3	177.17	162.73	159.17	155.52
4	306.09	297.56	289.38	280.77
5	419.75	413.75	408.37	403.03
6	487.67	481.76	477.15	472.48
7	679.39	670.82	662.71	654.28
8	793.69	786.73	780.53	744.45
9	1079.6	974.59	970.93	967.21
10	1186.1	1177.4	1169.1	1160.5

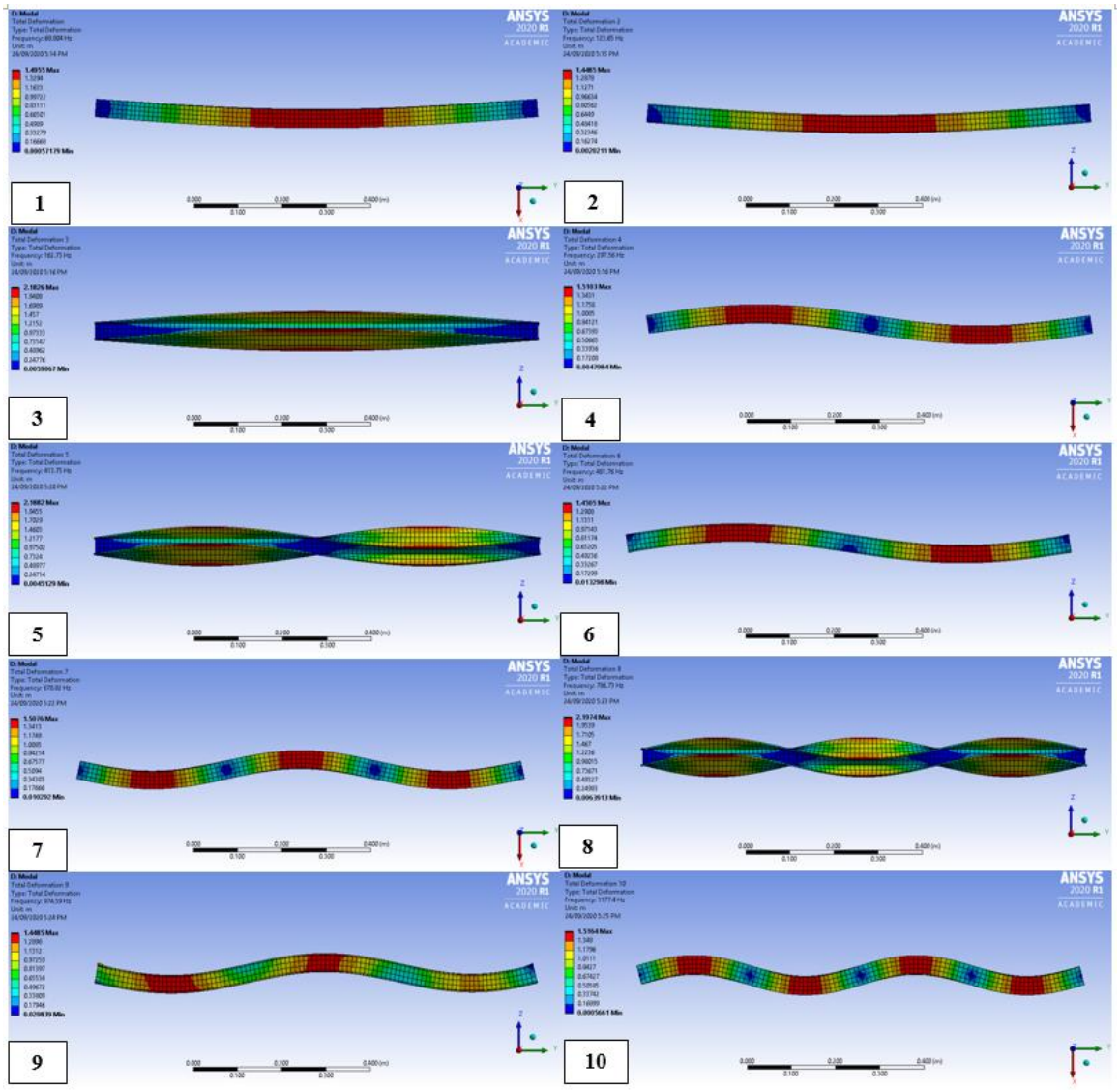

Figure 4.1. The mode shape of the I beam with an applied load of 4400N.

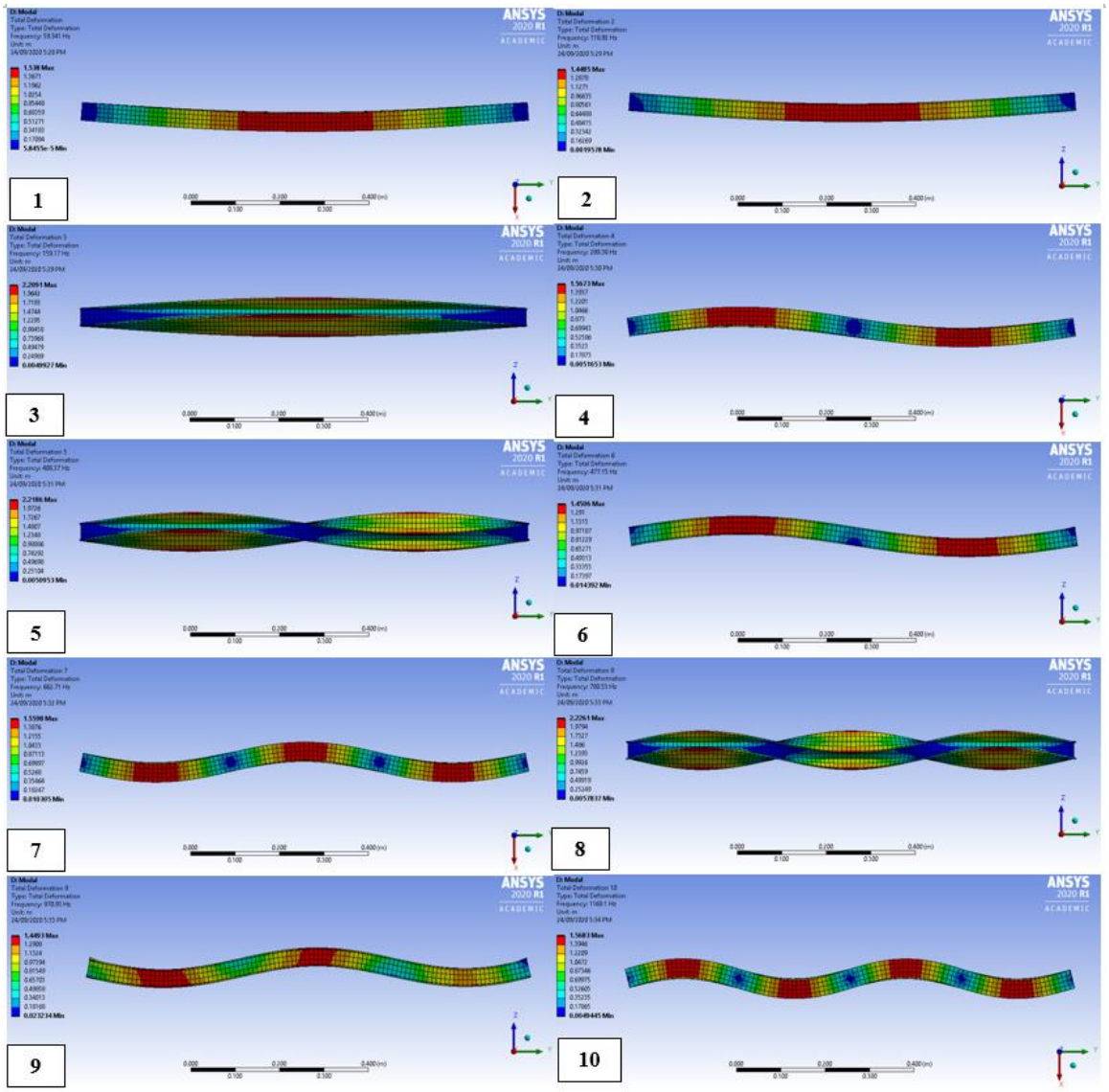

Figure 4.2. The mode shape of the I beam with an applied load of 8800N.

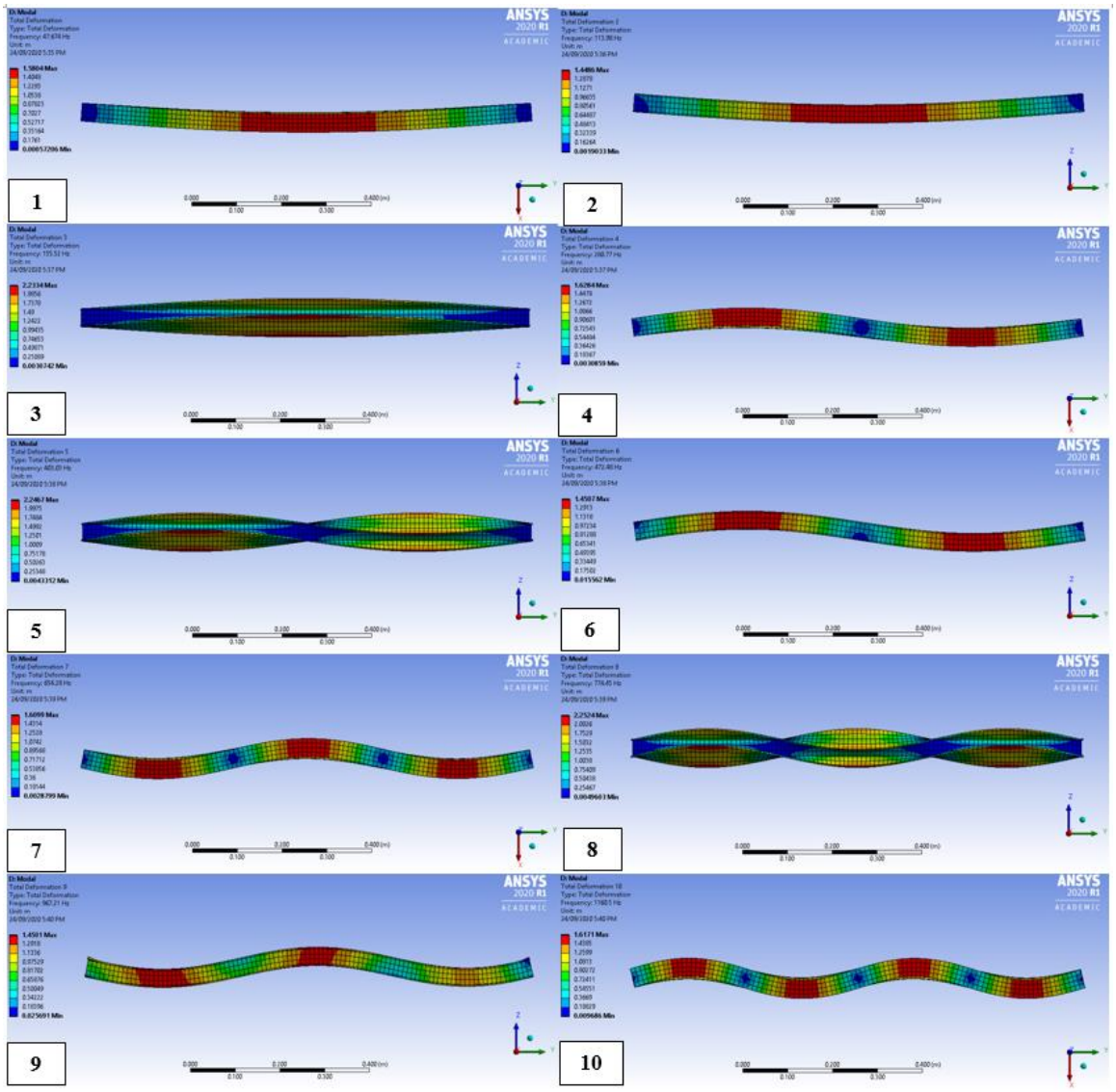

Figure 4.3. The mode shape of the I beam with an applied load of 13201N.

4.1.3 Laboratory Experiment

First, the experiments for measuring the natural frequency are carried out in accordance with the experimental method explained in Chapter 3. By observing the frequency spectrum on Waveform Editor, it is found that frequencies around 70Hz and 300Hz can always be found, such as Figure 4.4. These frequencies match with the first and second

frequencies in horizontal direction obtained by the Rayleigh-Ritz method, whose difference is about 10%.

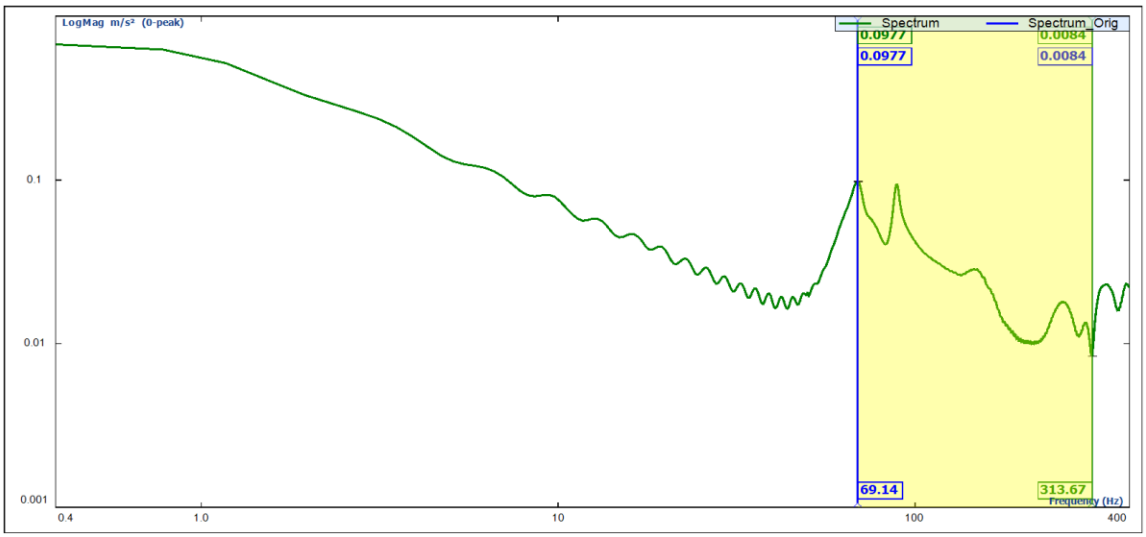

Figure 4.4. The spectrum of simply-supported I beam.

Another vibration test is also carried out to measure the natural frequencies of the I beam under the applied load of 4400N, 8800N, and 13201N. The results are given in Table 4.5. Positions 1 to 3 in Table 4.5 are the left end, the center and the right end of the I beam respectively (refer to Figure 3.3). The X-axis direction is along the axis of the beam, the Y-axis direction is vertical to the horizontal plane, and the Z-axis direction is parallel to the horizontal plane. The specific direction is shown in Figure 4.5.

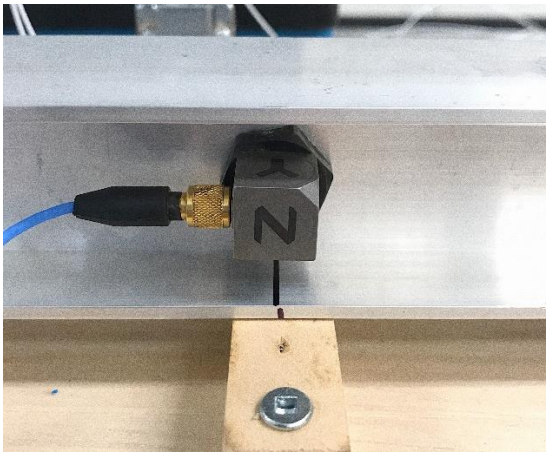

Figure 4.5. The axis orientation of the accelerometer.

Table 4.5. The lab results of the I beam (Hz).

			1st	*2nd*	*3rd*	*4th*	*5th*
4400N	Position1	Y axis	71.09	148.44	173.44	260.55	378.91
		Z axis	69.14	147.27	178.13	233.2	358.2
	Position2	X axis	71.88	147.27	174.22	226.17	357.81
		Y axis	71.09	147.27	171.88	281.64	347.66
	Position3	X axis	65.63	131.25	175.78	248.05	355.8
		Y axis	65.23	145.31	173.44	266.41	383.59

			1st	*2nd*	*3rd*	*4th*	*5th*
8800N	Position1	X axis	71.88	158.59	178.52	254.3	363.67
		Y axis	69.92	148.44	175	237.11	389.84
		Z axis	66.41	158.59	185.95	257.42	367.19
	Position2	X axis	67.97	142.97	186.72	241.02	363.28
		Y axis	68.75	142.97	173.44	239.06	375.39
		Z axis	67.97	137.11	172.66	240.63	373.05
	Position3	Y axis	69.53	153.52	175.78	264.06	384.77

			1st	*2nd*	*3rd*	*4th*	*5th*
13201N	Position1	Z axis	65.63	135.94	195.31	259.83	341.41
	Position2	X axis	64.06	151.17	175	283.98	366.41
		Y axis	70.31	144.92	175	275.78	366.8
	Position3	X axis	65.63	157.81	192.97	272.27	364.84
		Y axis	67.97	150.78	176.56	262.11	365.23

4.1.4. Discussion

Figure 4.6 displays the relationship between the axial load and the natural frequency. It can be clearly seen that as the axial load increases, the natural frequency gradually decreases. In the MATLAB experiment, when the rail axial load is 4400N, the natural frequency of 69Hz is obtained. In the ANSYS experiment, when the rail axial load is 4400N, the natural frequency of 68.804Hz is obtained. When the applied load is 4400N, the natural frequency obtained by the CoCo-80 is 69.14Hz. The percentage of difference between the natural frequencies obtained by ANSYS and the natural frequency obtained by MATLAB is 0.2%. The percentage of difference between the natural frequencies obtained by ANSYS and the natural frequency obtained by the laboratory test is 0.4%.

From Figure 4.6, the results of ANSYS and MATLAB fit well. But as the applied load increases, the difference between the results obtained by ANSYS and MATLAB gradually increases. The reason for the slight difference may be that the beam theories of the two numerical analysis methods are somewhat different. For the Rayleigh-Ritz method, the Euler-Bernoulli beam theory is used, which is based on one-dimensional beam model. For the finite element analysis method, a three-dimensional model is used in ANSYS. The theories of different dimension models have caused these slight differences.

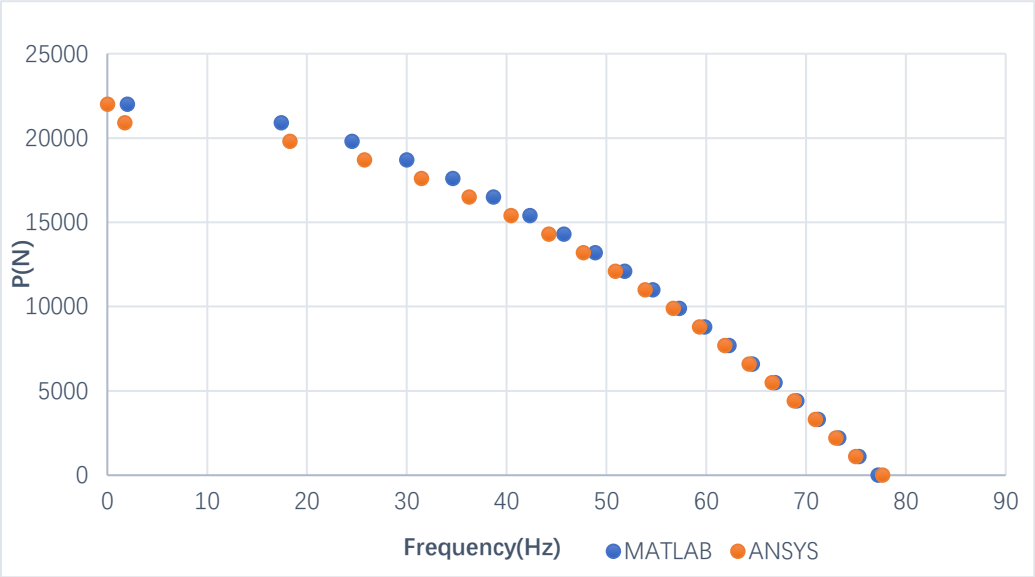

Figure 4.6. The relationship between the axial load and the natural frequency.

For the laboratory test, it can be seen from Table 4.7 that the natural frequency can be acquired at three positions. And under the same load, the frequencies obtained at different positions are very similar. As can be seen from the spectrograms in Appendix II, in addition to the natural frequency of the beam itself, other peaks can also be observed. The reason for this may be that the vibration frequency generated by the clamp used to fix the beam is also captured. In addition, the friction between the laboratory desktop and the clamp is small, and it is very easy to move during the excitation test. In order to reduce the influence of these factors on the experiment, some rubber pads can be placed on the bottom of the clamp to increase the friction during the experiment.

Figure 4.7 gives the relationship between the axial load and the natural frequency, and at the same time, the degree of fit between the experimental results of ANSYS and laboratory is also shown in the figure. The reason for the difference may be that the boundary condition is not exactly simply supported. It is between the simply supported and clamped

conditions. That may cause the increase in the nature frequency. In addition, the accuracy of the measurement of the axial force applied by the bottle jack is limited. The influence of noise in the laboratory, and errors in signal acquisition may also cause the difference.

Both the numerical method and experimental method shows the relationship between the natural frequency and the axial force, which is that the natural frequency deceases as the axial load increases.

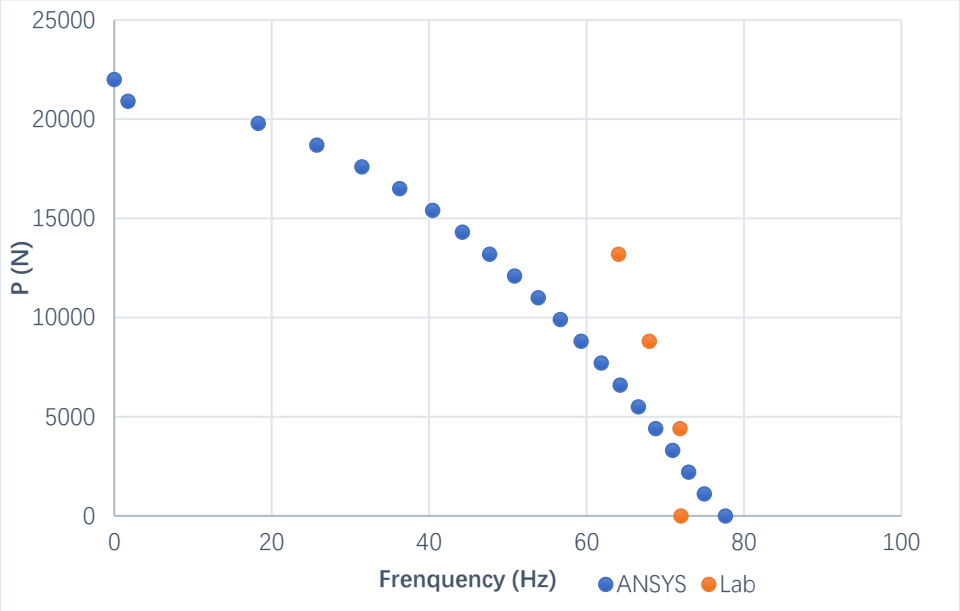

Figure 4.7. The degree of fit between the experimental results of ANSYS and laboratory.

4.2. T beam

4.2.1 The Rayleigh-Ritz Analysis

Refer to the parameters in Table 3.1, the properties of the T beam are given as $E = 6.95 \times 10^{10}$Pa, $I_y = 4.15 \times 10^{-9}\, m^4$, $I_z = 8.25 \times 10^{-9}\, m^4$, M = 0.383 Kg/m and $A = 1.42 \times 10^{-4} m^2$. The theoretical results of critical load and natural frequencies are shown in Table 4.6 and Table 4.7.

Table 4.6. The theoretical critical load of the T beam.

Buckling load(N)		
	P(Iz)	**P(Iy)**
K=1	5659	2846.6

Table 4.7. The theoretical natural frequencies of the T beam.

Frequency(Hz)		
Mode	***f*(Iz)**	***f*(Iy)**
1	60.777	43.105
2	243.10	172.42
3	546.99	387.95

The 20%, 40%, and 60% of critical buckling load were included into MATLAB for calculation. And the natural frequencies are obtained, and they are shown in Table 4.8.

Table 4.8. The natural frequencies of T-beam obtained using MATLAB (Hz).

P(N) / Mode	568.8	1173.6	1706.4
1	38.559	33.4	27.281
2	57.641	54.325	50.793
3	168.06	163.58	158.97
4	240.03	236.92	233.76
5	383.62	379.24	374.81
6	543.93	540.85	537.75
7	685.37	681.02	676.65
8	969.37	966.31	963.23

4.2.2 The Finite Element Method Analysis

To build a simply supported beam, two remote displacements are added on the surfaces at both ends. After that, the normal stress and eigenvalue of buckling can be solved. The number of elements used is 1200. Normal force is 219.86N and the first mode eigenvalue is 11.986. According to Eq.2.1, the critical buckling load is 2635.2N and the first mode of natural frequency is 44.449Hz. These values agree well with the values given by the Rayleigh-Ritz method.

Thereafter, loads are applied on the surfaces at both ends. The values of loads are 773N, 1154.7N, and 1450.7N. The model can be solved to obtain the natural frequencies and mode shapes. The 1st to 10th modes of frequency are shown in Table 4.9. Figure 4.8- 4.10 shows the mode shapes under the axial load of 773N, 1154.7N, and 1450.7N respectively. The first mode shape under 773N is quite similar to the first mode shapes under 1154.7N and 1450.7N. The other modes are the same as this. In the 1st, 3rd, 6th, and 9th modes, the T beam vibrates along the horizontal direction. The beam vibrates along the vertical direction at the 2nd, 4th, and 7th modes. Twist can be seen in the 5th, 8th, and 10th modes.

Table 4.9. The natural frequency of T-beam obtained using ANSYS (Hz).

P (N) / Mode	0	773	1154. 7	1450. 7
1	44.449	36.609	33.168	30.229
2	78.115	56.186	53.99	52.225
3	169.9	162.59	159.71	157.44
4	240.83	235.44	233.38	231.78
5	290.08	289.23	288.89	288.63
6	369.34	362.49	359.79	357.69
7	553.82	527.25	525.21	523.63
8	588.04	586.25	585.55	585.01
9	626.52	620.32	617.81	615.86
10	1186.1	900.00	899.81	898.89

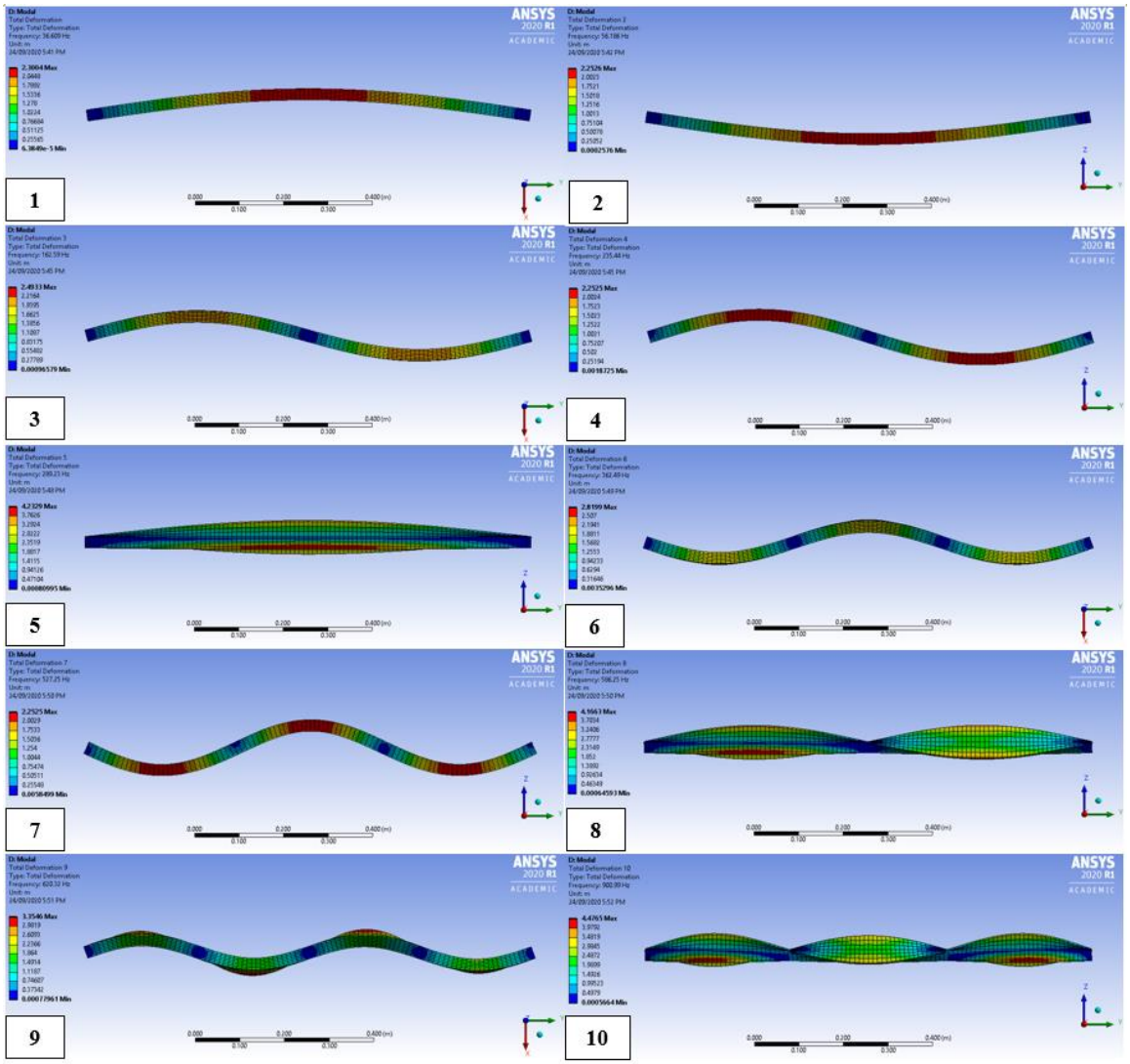

Figure 4.8. The mode shape of the T beam with an applied load of 773N.

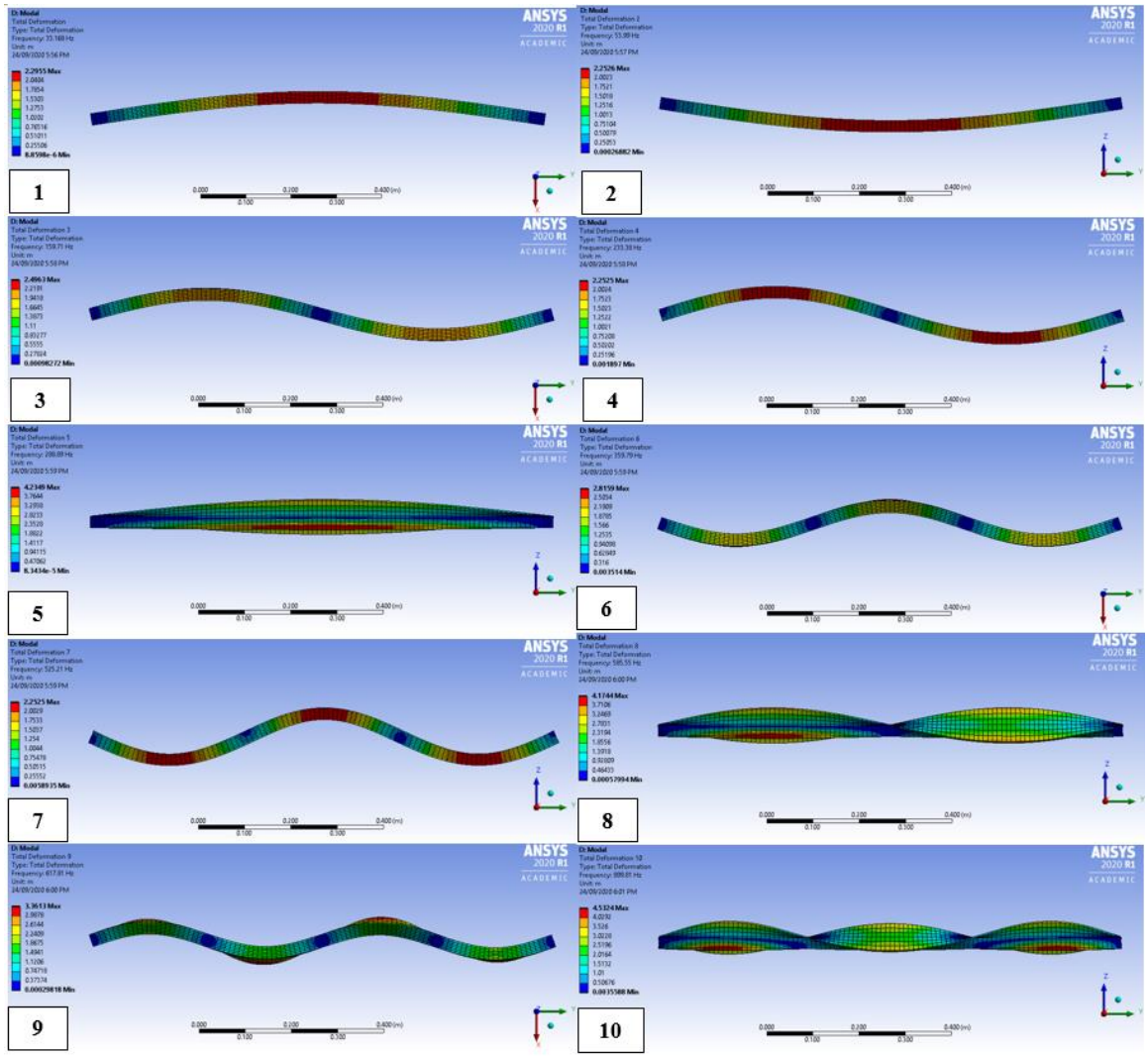

Figure 4.9. The mode shape of the T beam with an applied load of 1154.7N.

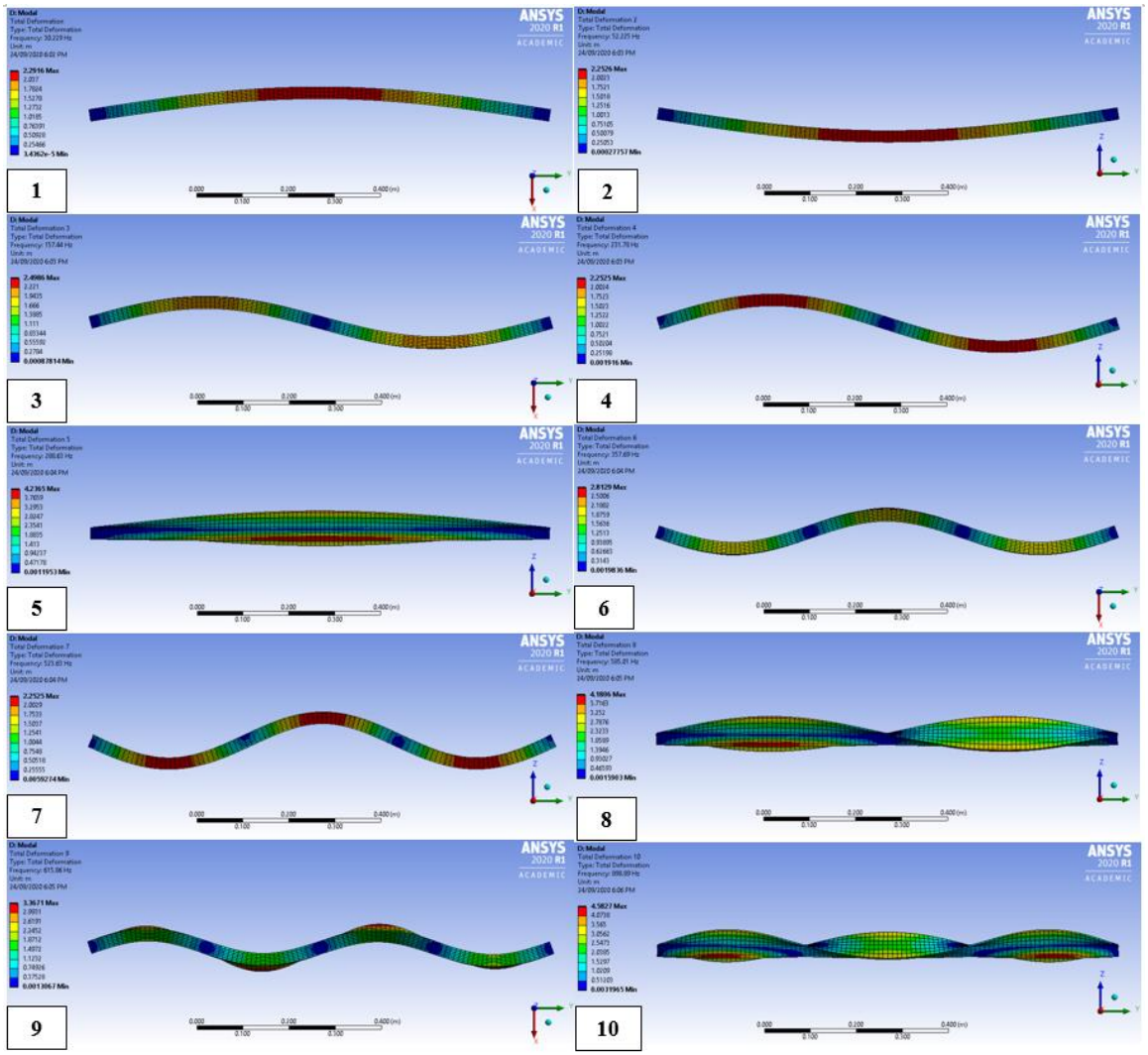

Figure 4.10. The mode shape of the T beam with an applied load of 1450.7N.

4.2.3 Laboratory Experiment

In previous experiments with the I-beam, it has been confirmed that the experimental results are close to the theoretical natural frequencies. And then the tests for measuring the natural frequencies of the T beam are carried out under the applied load of 773N, 1154.6N, and 1450.7N. Table 4.10 summarizes all the experimental results obtained by laboratory tests. All of the spectrums are shown in Appendix II.

Table 4.10. The lab results of the T beam (Hz).

		1st	2nd	3rd	4th	5th	6th
773N	Position1	50.78	63.28	187.89	251.95	274.61	350.78
	Position2	48.83	80.47	187.11	245.7	312.89	353.91
	Position3	50.78	69.53	182.81	226.17	271.09	343.75
1154.67N	Position1	49.22	72.27	161.22	235.55	273.05	350.39
	Position2	48.83	142.97	167.19	238.29	271.09	370.31
	Position3	50.78	76.56	190.23	264.45	287.89	344.14
1450.7N	Position1	50.39	64.68	197.27	243.75	269.53	374.61
	Position2	48.83	68.75	160.16	237.11	309.38	375.78
	Position3	50.78	66.8	196.88	244.92	259.38	345.31

4.2.4. Discussion

The same conclusion as we obtained for the I beam may be drawn. When the applied load is 568.8N, the natural frequency for the first mode calculated by MATLAB is 38.6Hz, and when the applied load is 773N, the first natural frequency solved by ANSYS is 36.609Hz, the first natural frequency captured by the CoCo-80 is 48Hz. When the applied load is 568.8N, the difference between the natural frequencies obtained by ANSYS and MATLAB is around 0.6%.

For the laboratory test, it can be seen from Table 4.10 that the natural frequencies can be acquired at three positions. And under the same load, the frequencies obtained at different positions are very similar. In addition, the first to sixth mode natural frequencies obtained by laboratory tests are close to the results solved by ANSYS.

The relationship between the axial load and the natural frequency is shown in Figure 4.11. It also shows the fit of the results obtained by ANSYS and MATLAB. From Figure 4.11, the results obtained by MATLAB agree well with the results obtained by ANSYS. And

about the results of ANSYS and lab tests, the relationship between the axial load and the natural frequency is displayed in Figure 4.12. From these two graphs, it can be seen that both methods show the relationship of that the natural frequency decrease as the axial load increases.

Using both the numerical method and the experimental method, the relationship of the natural frequencies and the axial forces can be obtained. For the numerical methods, it has the same situation as the I beam, the beam theories used in the Rayleigh-Ritz method and the Finite Element Method are different, which may cause the slight difference between the results.

The laboratory results are significantly different from the other two results. That may cause by the boundary condition of the beam which is between the simply supported condition and clamped condition. Moreover, in addition to the boundary condition, the limited accuracy for measuring the stress, and a slight inclination of the planes at both ends of the beam may also cause the difference. During the experiment, it was seen that the plane of the end of the beam is not completely perpendicular to the bottom surface, which may be caused by the factory cutting. The inclination of the planes at both ends may cause uneven stress distribution, resulting in a large difference between the frequency obtained by the experiment and the frequency obtained by ANSYS.

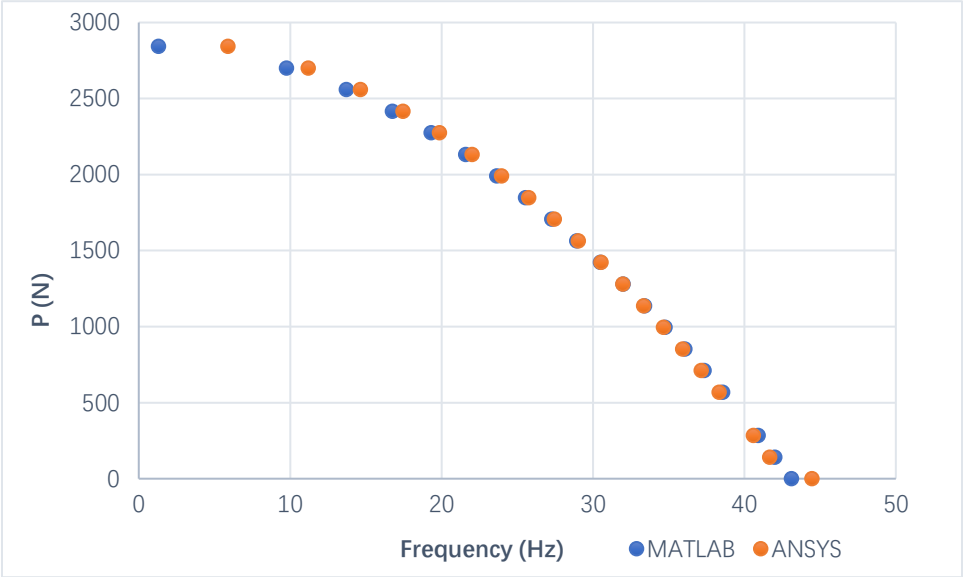

Figure 4.11. The relationship between the axial load and the natural frequency.

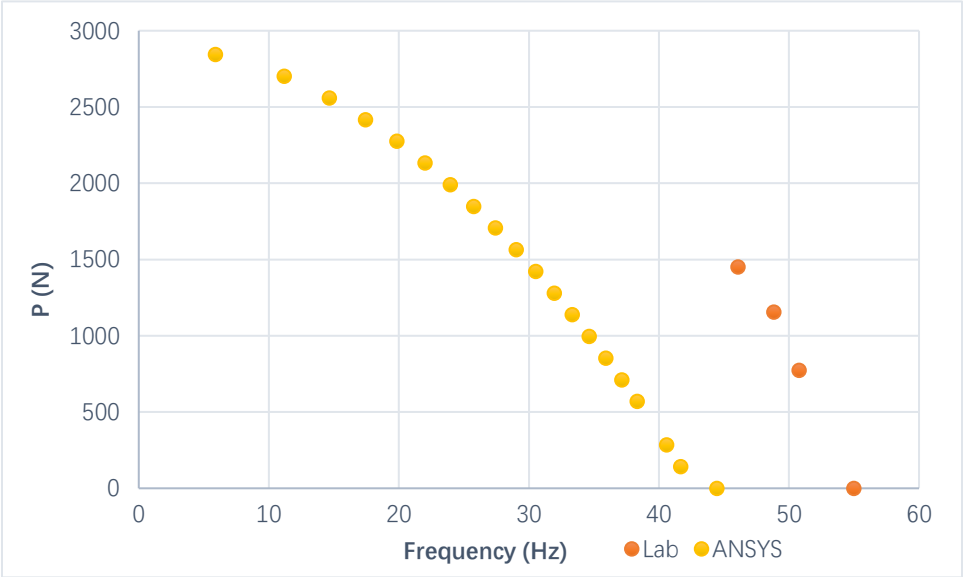

Figure 4.12. The degree of fit between the experimental results of ANSYS and laboratory.

4.3 Steel beam

4.3.1 The Rayleigh-Ritz Analysis

Refer to the parameters in Table 3.1, the properties of the steel beam are given as $E = 2.06 \times 10^{11}$ Pa, $I_y = 2.08 \times 10^{-9}\, m^4$, $I_z = 1.3 \times 10^{-8}\, m^4$, M = 1.96 Kg/m and $A = 2.5 \times 10^{-4} m^2$. The theoretical results of critical load and natural frequencies for the simply supported beam are obtained by using MATLAB. They are shown in Table 4.11 and Table 4.12.

Table 4.11. The theoretical critical loads of the steel beam.

Buckling load(N)		
	P(Iz)	**P(Iy)**
K=1	26431	4228.9

Table 4.12. The theoretical natural frequencies of the steel beam.

Frequency(Hz)		
Mode	***f*(Iz)**	***f*(Iy)**
1	58.063	23.225
2	232.25	92.903
3	522.56	209.02

To find a relationship between frequency changes and axial loads, input the 20%, 40%, and 60% of the critical buckling load to MATLAB. The natural frequencies are obtained and they are shown in Table 4.13.

Table 4.13. The natural frequencies of the steel beam obtained using MATLAB (Hz).

P(N) / Mode	847	1694	2541
1	20.706	17.908	14.583
2	57.124	56.171	55.201
3	90.312	87.887	85.394
4	231.31	230.38	229.44
5	206.17	203.81	201.41
6	521.63	520.71	519.76
7	368.35	366.01	363.63
8	928.07	927.14	926.21

4.3.2 The Finite Element Method Analysis

After building a simply supported beam, the normal stress and eigenvalue of buckling can be solved with ANSYS. The number of elements used for this analysis is 2000. Normal force is 1200N and the first mode eigenvalue is 3.4267. According to Eq.2.1, the critical buckling load is 4112N and the first mode of natural frequency is 26.011Hz. These values agree well with the values given by the Rayleigh-Ritz method.

The values of loads are set to 847N, 1694N, and 2541N on the surfaces at both ends. The model is solved to obtain the natural frequencies and mode shapes. The 1st to 10th modes of frequency are shown in Table 4.14. Figures 4.13-4.15 show the mode shapes under the axial load of 847N, 1694N, and 2541N respectively. It can be seen from that, each mode shape under different applied load are very similar. In the 1st, 3rd, 4th, 6th,8th and 9th modes, the steel beam vibrates along the horizontal direction. And in the 2nd, 5th, 7th and 10th modes, the beam vibrates along the vertical direction. No twist occurs in any mode.

Table 4.14. The natural frequencies of the steel beam obtained using ANSYS (Hz).

P(N) / Mode	0	847	1694	2541
1	26.011	20.391	17.547	14.143
2	58.482	56.211	55.247	54.266
3	94.784	89.093	86.64	84.115
4	209.06	203.24	200.85	198.42
5	229.28	226.97	226.02	225.07
6	368.76	362.69	360.31	357.92
7	511.63	509.14	508.2	507.26
8	573.65	566.82	564.46	562.09
9	823.41	815.66	813.3	810.94
10	902.24	866	865.9	865.8

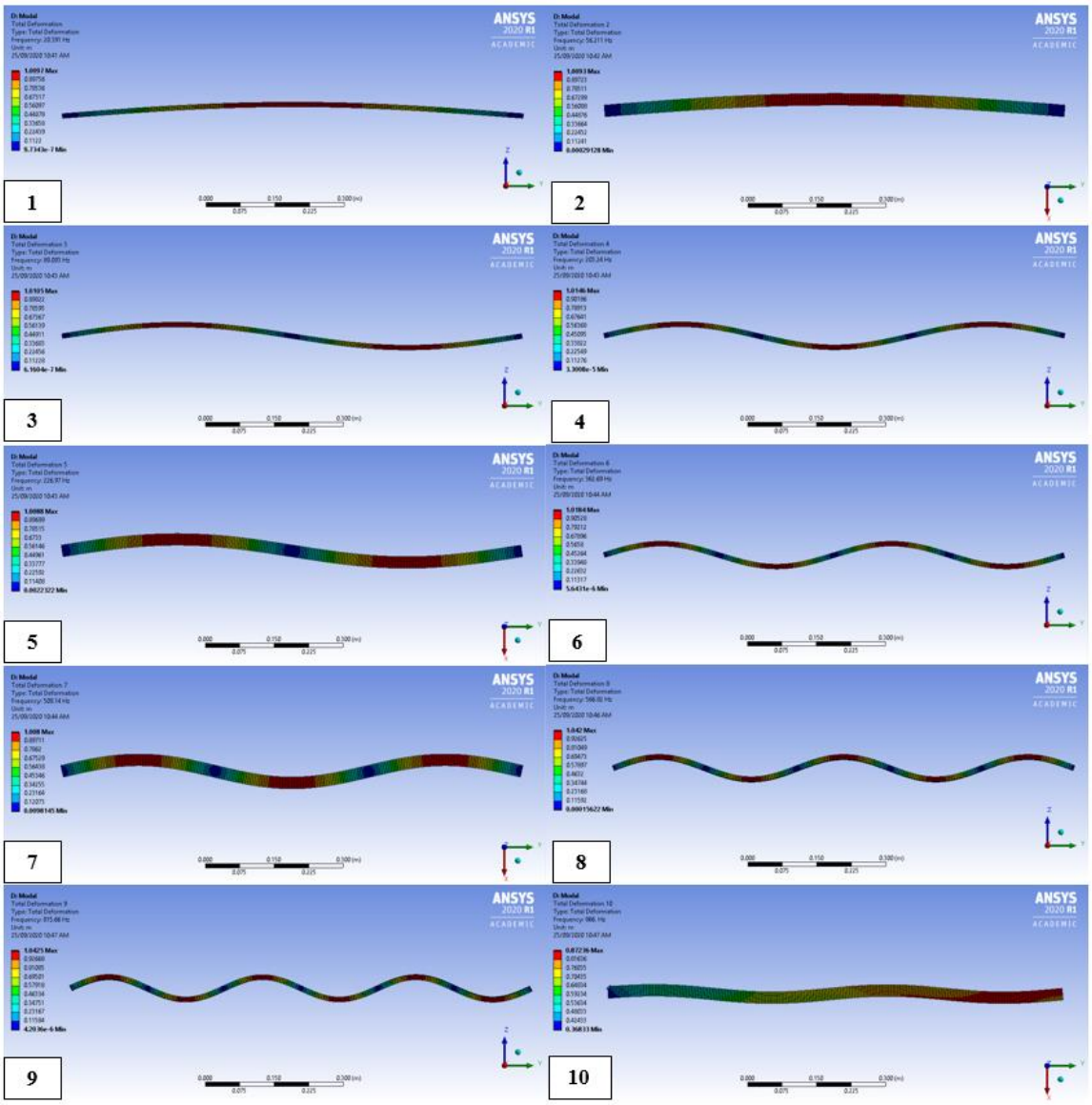

Figure 4.13. The mode shape of the steel beam with an applied load of 847N.

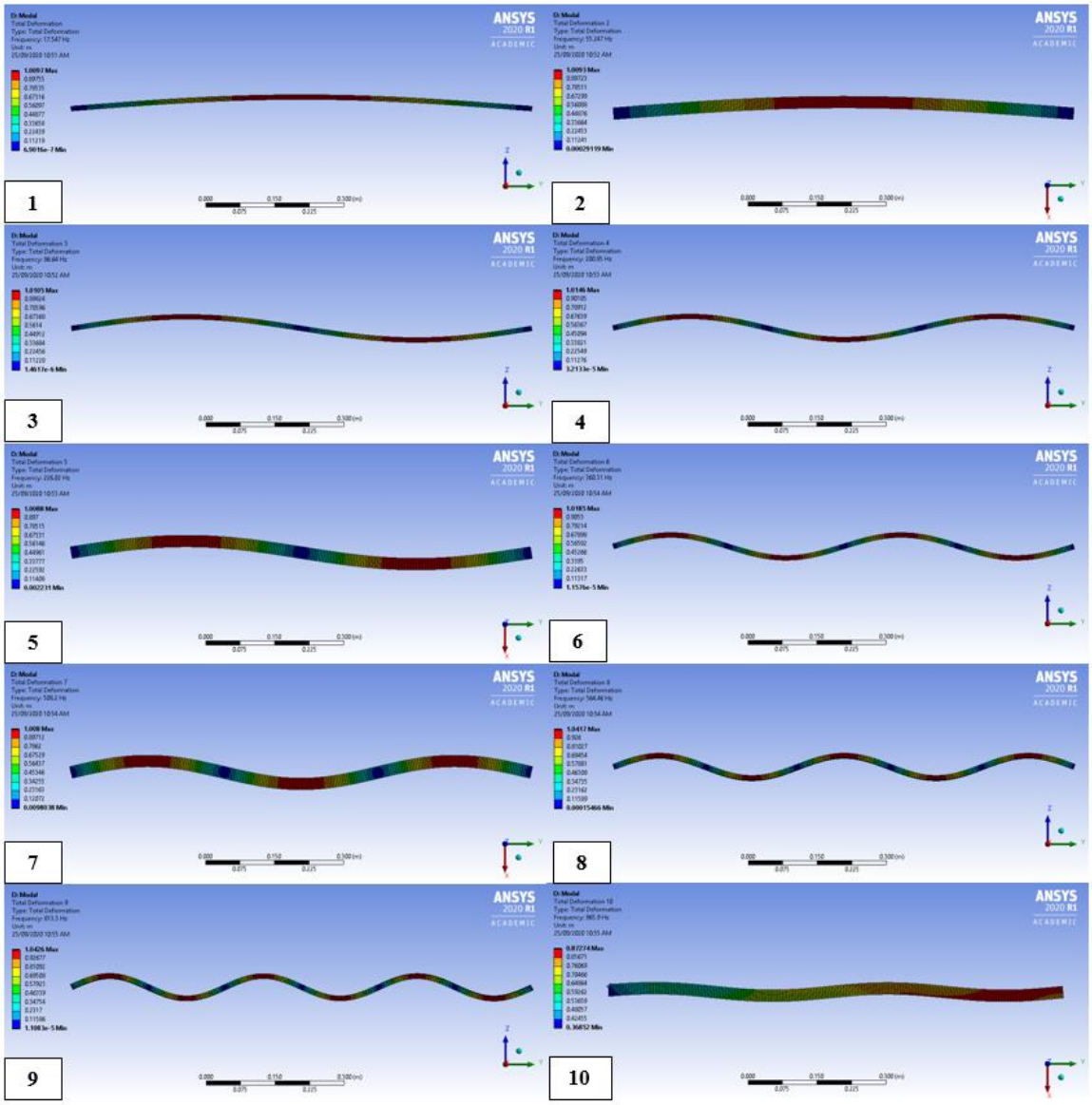

Figure 4.14. The mode shape of the steel beam with an applied load of 1694N.

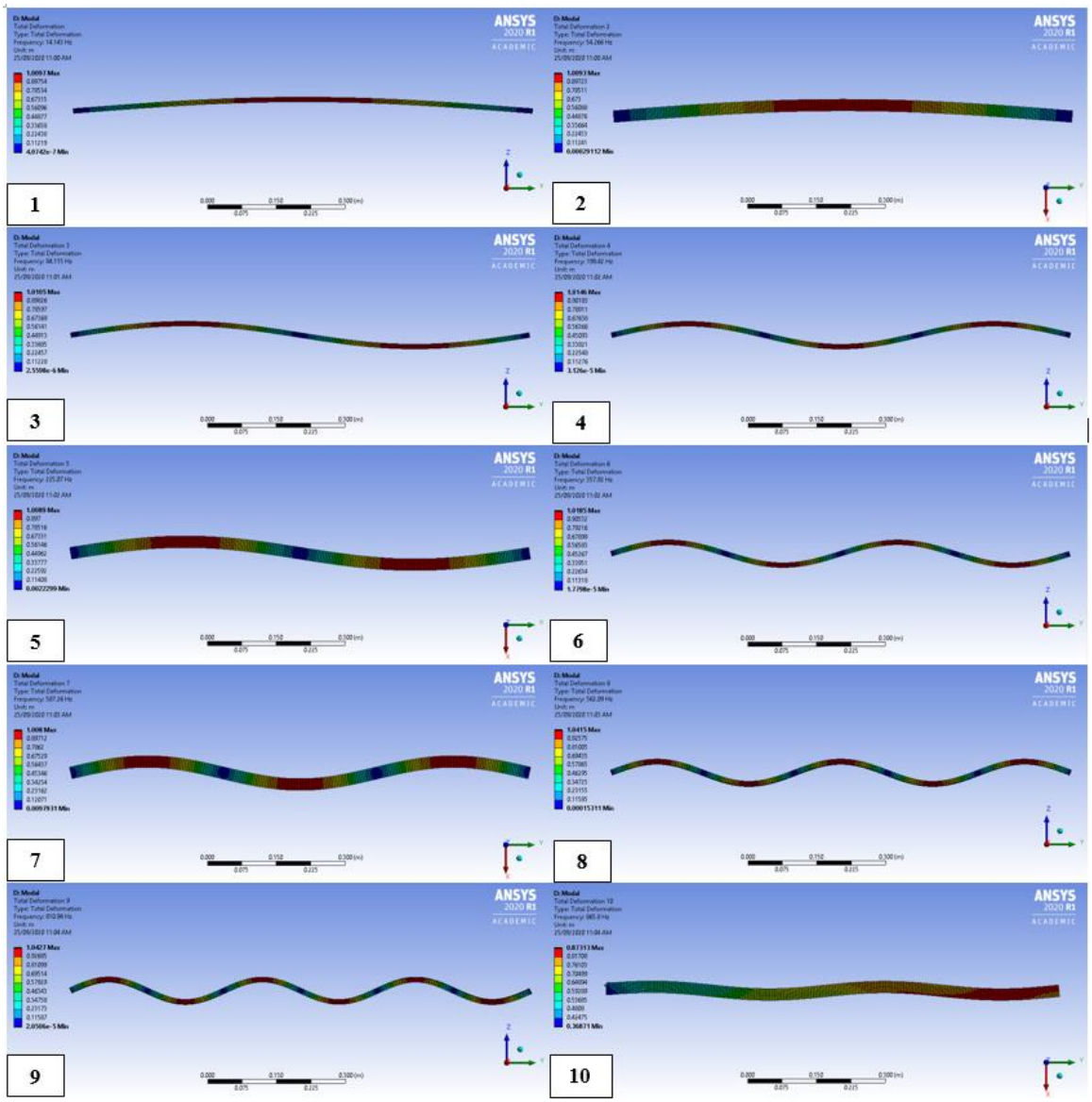

Figure 4.15. The mode shape of the steel beam with an applied load of 2541N.

4.3.3 Laboratory Experiment

Similarly to the previous test on the I beam, firstly we test the natural frequencies of the steel beam under the applied load of 864N, 1694N, and 2541N. Table 4.15 summarizes all

the experimental results obtained by laboratory tests. And all of the spectrums are shown in Appendix II.

Table 4.15. The lab results of the steel beam (Hz).

		1st	2nd	3rd	4th	5th	6th
864N	Position1	22.66	76.56	100	201.17	238.28	396.48
	Position2	28.13	53.91	91.08	171.09	217.19	381.64
	Position3	19.92	61.33	91.8	170.31	218.36	379.69
1694N	Position1	26.56	58.98	99.222	198.83	233.2	396.09
	Position2	26.17	69.53	113.28	181.64	253.52	379.3
	Position3	25.39	58.2	98.83	182.81	232.81	394.92
2541N	Position1	24.22	58.98	99.22	217.97	235.16	385.94
	Position2	24.22	56.25	100	191.41	237.89	377.73
	Position3	24.61	78.13	99.61	169.92	232.42	333.59

4.3.4 Discussion

The same conclusion as the I beam and T beam may be drawn. When the applied load is 864N, the first natural frequency calculated by MATLAB is 20.7Hz, the first natural frequency solved by ANSYS is 20.391Hz, and the first natural frequency captured by the CoCo-80 is 22Hz. The difference between the natural frequency obtained by ANSYS and MATLAB is around 1%. The difference between the natural frequencies obtained by ANSYS and laboratory is around 7%. The difference is still within an acceptable range.

For the laboratory test, it can be seen from Table 4.15 that the natural frequency can be acquired at three positions. And under the same load, the frequencies obtained at different positions are very similar. In addition, the first to sixth mode natural frequencies obtained by laboratory tests are close to the results solved by ANSYS.

For these three methods, the relationship between the axial load and the natural frequency is shown in Figure 4.16. It also shows the fit of the results. Using both the numerical method and the experimental method, the relationship of the natural frequencies and the axial forces can be obtained. As the applied load increases, the natural frequency gradually decreases. The finite element method has a good agreement with the Rayleigh-Ritz method.

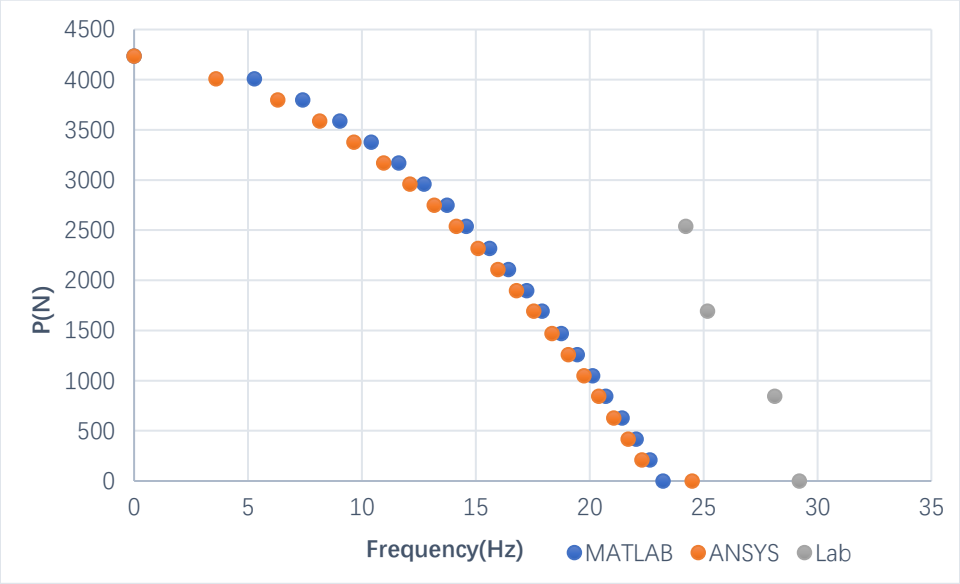

Figure 4.16. The relationship between the axial load and natural frequency.

4.4. Summary

From all the experimental, the relationships between the natural frequency and the axial load can be obtained.

From Appendix II, it can be seen that the spectrum obtained by using the steel beam will have more obvious and clear peaks than the other two beams. That may be caused by the different damping ratios of different materials and cross-sections. The damping of steel is lower than aluminum.

For the laboratory test, there are some differences for all the beams we tested from the results of the numerical methods, which may be caused by uneven axial force in the beam. Ideally, the axial force of the beam should be uniform, but the experimental device uses the bottle jack on the left to apply axial pressure to the beam, which usually causes greater pressure on both ends. This was observed by the strain recorder. During the load application process, the values displayed by the strain gauges at the three positions are always different. Table A3.1 shows the strain values applied to each beam during the experiment. When the strains corresponding to the three positions are different, the strain value corresponding to the center position of the beam will be adopted. And in the stress distribution diagram of ANSYS (Figure 4.17), it can be seen that the force on the entire beam is uneven. The normal stress is highest on the side where the force is applied. The closer to the other side, the normal stress gradually decreases.

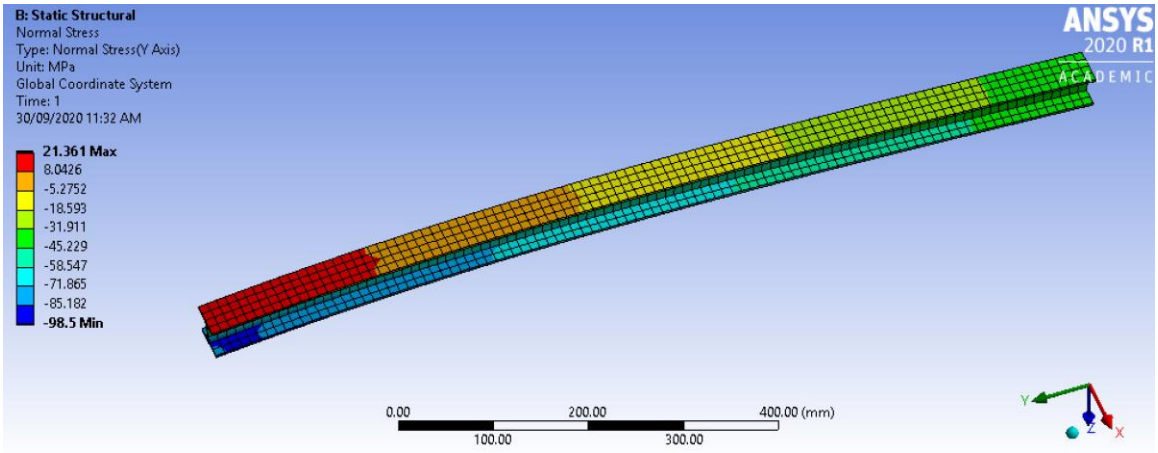

Figure 4.17. Schematic diagram of normal force distribution in the I beam.

Chapter 5: Acoustic Emission Technology

Based on the success of the detection methods mentioned earlier, we carried out extended research on a new experimental detection method, Acoustic emission (AE) technology, which is a kind of new detect method [39-41]. Compared with other traditional detection methods, acoustic emission technology has the advantages of unlimited geometric shapes, high sensitivity, dynamic detection, and real-time monitoring [42, 43]. Therefore, many studies were carried out to detect rail vibration and monitor railway track performance by acoustic emission technology.

5.1 Experimental method

The model used for the extended experiment is the steel beam, Replace the accelerometer used before with a microphone sensor (Figure 5.1) developed by Virtins Technology, and connect the microphone sensor to the CoCo-80. The mode used is the Frequency Response Function (FRF) mode. The sensitivity of the microphone sensor is 36.3mv/Pa. The other steps of the experiment are the same as mentioned in Chapter 3.

Figure 5.1. The schematic diagram of the microphone sensor

5.2 Results and Discussion

The natural frequencies of the steel beam are detected with the applied load of 847N, 1694N, and 2541N. Table 5.1 summarizes the experimental results obtained by using a microphone sensor, and all of the spectrums are shown in Appendix II. When the applied load is 847N, $f_1 = 24.22Hz, f_2 = 70.7Hz,$ and $f_3 = 110.16Hz$. When the applied load is 1694N, $f_1 = 23.05Hz, f_2 = 34.38Hz,$ and $f_3 = 104.3Hz$. When the applied load is 2541N, $f_1 = 23.05Hz, f_2 = 35.94Hz,$ and $f_3 = 100Hz$.

Table 5.1 The natural frequency of the steel beam using the microphone sensor (Hz).

	1st	2nd	3rd	4th	5th	6th
847N	24.22	70.7	110.16	217.19	235.94	396.09
1694N	23.05	34.38	104.3	200	241.8	343.75
2541N	23.05	35.94	100	176.17	200	393.36

Compare with the frequency of the steel beam by using the accelerometer, the percentages of difference are 13.8%, 11.9%, and 4.8% with the applied load of 847N, 1694N, and 2541N respectively. From Figure 5.2, it can be seen that the results obtained by using the microphone sensor have a reasonable agreement with the results acquired by using an accelerometer.

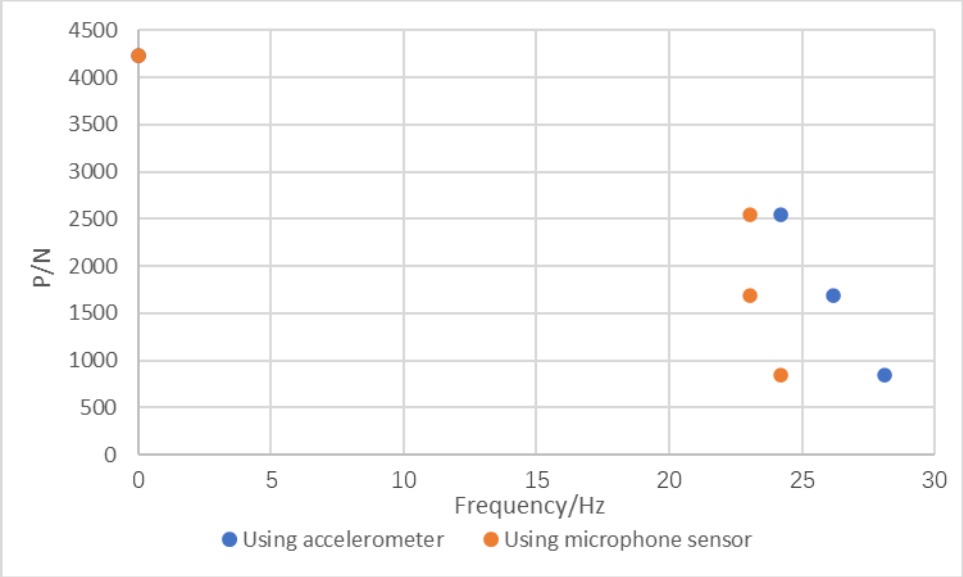

Figure 5.2. The degree of fit between the natural frequency obtained by using accelerometer and microphone sensor.

The spectrums of the steel beam with the applied load of 847N are shown in Figure 5.3. Compared to the spectrum obtained by using the microphone (Figure 5.3a) with that of using an accelerometer (Figure 5.3b), it illustrates that the spectrum obtained by using the microphone sensor has more peaks. Except for the peak corresponding to the frequency of the beam itself, the other peaks should be caused by noise. And the same as mentioned before, the vibration of the clamp still makes influences on it. The unknown peaks are mostly between 100-400 Hz. This may be because the high-frequency region is more significantly affected by noise [44].

In addition to the frequencies of the beam, some peaks can always be captured and are not affected by the applied load. For example, the corresponding peaks can always be found at 17.97Hz and 46.88Hz. In order to confirm the noise, we also carried out a frequency capture test for the clamp by using the microphone sensor, whose spectrum is shown in

Figure 5.4. A peak can be found at 17.97Hz, it may be said that the source of noise with a frequency of 17.97 Hz is the clamp.

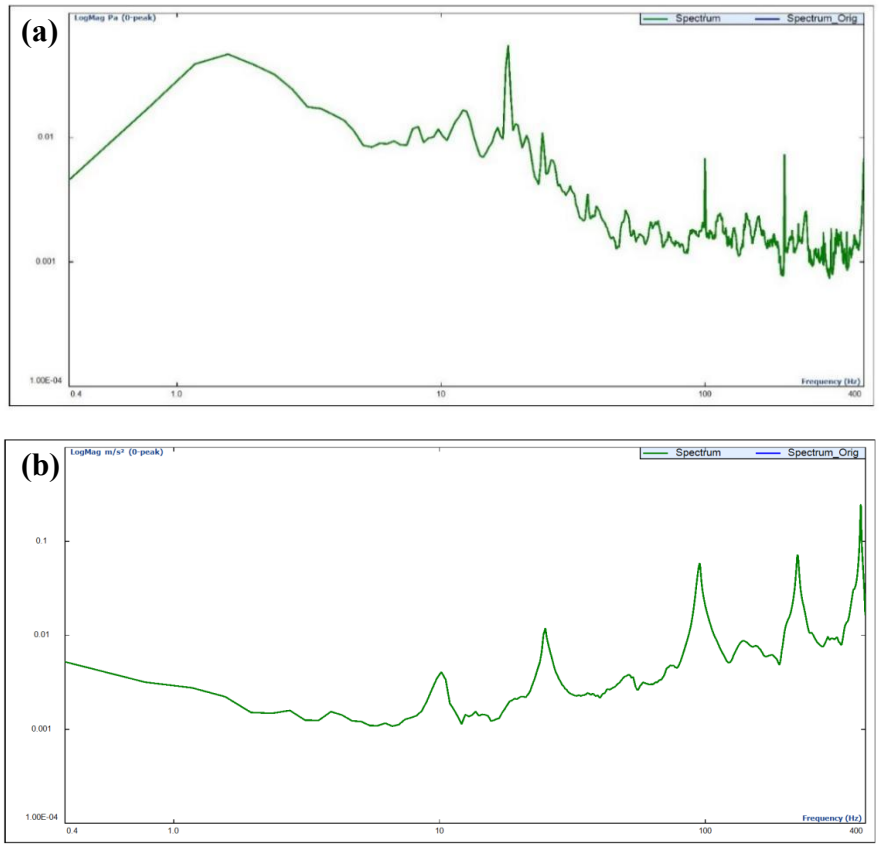

Figure 5.3. The spectrogram of the steel beam with the applied load is 847N (a) using the microphone sensor, (b) using an accelerometer.

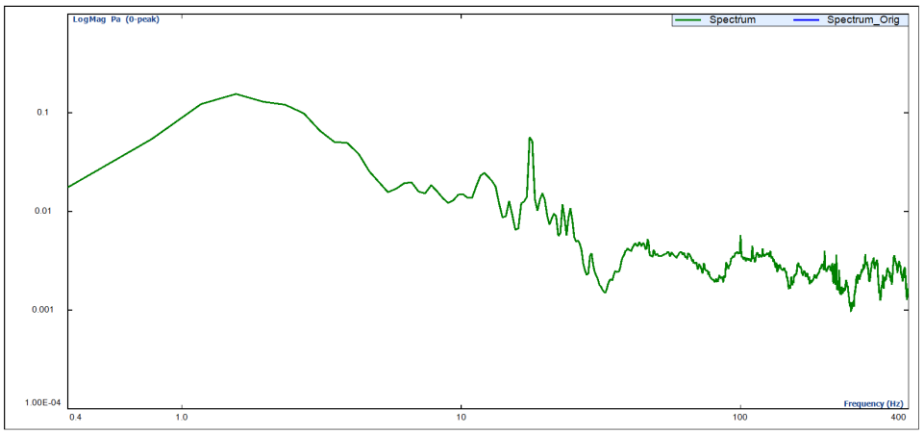

Figure 5.4. The spectrogram of the clamp.

Moreover, the movement of laboratory personnel or some working machines will affect the signal capture. In order to accurately obtain the natural frequencies of the beam, some signal processing may be needed. The noise can be attenuated by some noise reduction algorithms, such as band-pass filter, Wiener deconvolution, low-pass filter, matching pursuit, and wavelet noise reduction algorithm [45].

Another method is to establish a noise signal clustering model to distinguish beam signals from noise signals as outliers [46]. When the number of noise samples is large enough, a reliable noise signal feature library can be established. When the feature of the acquired signal belongs to the established noise feature library, it can be regarded as a noise signal. The unknown signal can be considered as an unknown noise signal or a beam signal.

5.3 Summary

The detection ability of acoustic emission technology is investigated using the acquired signals. The method using the microphone sensor to detect the natural frequencies of the

axially loaded beam is possible. This can provide an idea for monitoring the stress in the railway track using acoustic emission technology. For future research, the experiments need to be conducted on actual railway tracks, and in-depth research on noise treatment should be made, which may lead to a more efficient and safer method for monitoring the conditions of railway tracks.

Chapter 6: Conclusion

The critical buckling load and natural frequencies can be successfully obtained by using the numerical and experimental methods. This shows that these two methods can be used to obtain the relationship between the natural frequency and the axial force.

With the Rayleigh-Ritz method, the natural frequencies of the beams subjected to the axial loads are calculated. The beam theory used in the Rayleigh-Ritz method is one-dimensional beam theory. The results obtained are closer to the results obtained by using ANSYS. Taking the I beam as an example, the percentage of difference between the natural frequencies obtained by ANSYS and the natural frequency obtained by MATLAB is 0.2%.

With the finite element method, the natural frequencies of the beams with the axial loads are obtained. Meanwhile, using this method, the mode shapes of each beam are also obtained. The beam theory used in the finite element method is three-dimensional beam theory. When the applied load increases, the results for the natural frequencies solved by ANSYS are slightly different from the results obtained by using MATLAB. The reason of the difference could be that the different beam theories are used in these two methods.

For the laboratory experiments, due to many environmental factors, some noticeable difference between the experiment results and the numerical results are observed. During the test, since the material of the clamp is steel, the frequency of the clamp may also be captured. In addition, the desktop on which the model is placed is relatively smooth, which may cause slight displacement during the experiment. The movement of laboratory personnel and the noise of the laboratory may also affect the experimental results. Although

the results of laboratory experiment are different from those of the numerical experiments, since there are more environmental factors, it might be the closest to the actual application

About the acoustic emission technology, the signal can be captured and the values of the natural frequencies obtained are similar to the values of the natural frequencies obtained using the accelerometer. This confirms the feasibility of the experiment and shows that the experiment can be used to measure the natural frequencies of the beam. This method is more affected by noise, and the signal needs to be post-processed to distinguish the frequencies of the noise from the natural frequencies of the beam.

By testing three simply supported beams of different shapes and materials, both critical loads and natural frequencies can be obtained. The practicability of the numerical method and laboratory experimental methods has been confirmed. Therefore, it may be possible to put these methods into practical use to simulate and detect the axial load and natural frequency of the rail. With further research, these methods would contribute to development of non-destructive testing methods for the railway tracks.

Reference

1. A. Strauss, S.K., F. Kopf, C. Capraru, K. Bergmeister, *Monitoring-based performance assessment of rail-bridge interaction based on structural reliability.* Structural Concrete, 2015. **16**: p. 342–355.
2. Lim, N.-H., N.-H. Park, and Y.-J. Kang, *Stability of continuous welded rail track.* Computers & Structures, 2003. **81**(22-23): p. 2219-2236.
3. Lu, C. and C. Cai, *Overview on safety management and maintenance of high-speed railway in China.* Transportation Geotechnics, 2020. **25**.
4. Sangiorgio, V., A.M. Mangini, and I. Precchiazzi, *A new index to evaluate the safety performance level of railway transportation systems.* Safety Science, 2020. **131**.
5. Takahashi, R., et al., *Integrated risk of rail buckling in ballasted tracks at transition zones and its countermeasures.* Soils and Foundations, 2019. **59**(2): p. 517-531.
6. Yang, G. and M.A. Bradford, *On train speed reduction in circumstances of thermally-induced railway track buckling.* Engineering Failure Analysis, 2018. **92**: p. 107-120.
7. Zhu, J. and M.M. Attard, *In-plane nonlinear localised lateral buckling under thermal loading of rail tracks modelled as a sandwich column.* International Journal of Mechanical Sciences, 2015. **104**: p. 147-161.
8. Hani Tabai, B., et al., *Evaluating the impact of train drivers' cognitive and demographic characteristics on railway accidents.* Safety Science, 2018. **110**: p. 162-167.
9. Leitner, B., *A General Model for Railway Systems Risk Assessment with the Use of Railway Accident Scenarios Analysis.* Procedia Engineering, 2017. **187**: p. 150-159.
10. Wang, D. and T. Zhang, *Engineering accidents in society: A comparison of Chinese and American railway accident investigation.* Technology in Society, 2015. **43**: p. 69-74.
11. Damljanović, V. and R.L. Weaver, *Laser vibrometry technique for measurement of contained stress in railroad rail.* Journal of Sound and Vibration, 2005. **282**(1-2): p. 341-366.
12. Vnenk, P. and B. Culek, *Measurement Methods of Internal Stress in Continuous Welded Rail.* Acta Polytechnica CTU Proceedings, 2017. **11**.
13. Szelazek, J., *Monitoring of thermal stresses in continuously welded rails with ultrasonic technique.* NDTnet, 1998. **3**.
14. Aw, K.C., W.D.J. Huang, and M.W.R.P. De Silva, *Evaluation of climatic vibration testing on plastic waterproof enclosure for electronic equipment using ANSYS® workbench.* Materials & Design, 2007. **28**(9): p. 2505-2510.
15. Das, P. and S.K. Sahu, *Experimental and numerical study on free vibration of cracked woven fiber glass/epoxy composite beam.* Materials Today: Proceedings, 2020.

16. Ashraff Ali, K.S., et al., *Analysis of composite leaf spring using ANSYS software.* Materials Today: Proceedings, 2020.
17. Chen, S., et al., *Modal vibration response of rice combine harvester frame under multi-source excitation.* Biosystems Engineering, 2020. **194**: p. 177-195.
18. Gómez-Guzmán, J.M., et al., *A MATLAB-based interface for the beam-transport system of an AMS facility.* Nuclear Instruments and Methods in Physics Research Section B: Beam Interactions with Materials and Atoms, 2013. **316**: p. 130-136.
19. Sahu, S.K. and P. Das, *Experimental and numerical studies on vibration of laminated composite beam with transverse multiple cracks.* Mechanical Systems and Signal Processing, 2020. **135**.
20. Sheng, X., et al., *Using the Fourier-series approach to study interactions between moving wheels and a periodically supported rail.* Journal of Sound and Vibration, 2007. **303**(3-5): p. 873-894.
21. Sokhal, S. and S. Ram Verma, *A Fourier wavelet series solution of partial differential equation through the separation of variables method.* Applied Mathematics and Computation, 2021. **388**.
22. Senjanović, I., et al., *Vibration analysis of rotating toroidal shell by the Rayleigh-Ritz method and Fourier series.* Engineering Structures, 2018. **173**: p. 870-891.
23. Jeong, S. and H.H. Yoo, *Nonlinear structural analysis of a flexible multibody system using the classical Rayleigh–Ritz method.* International Journal of Non-Linear Mechanics, 2019. **110**: p. 69-80.
24. Shunichi TAKAHASHI, T.S. and Y.H. Yasuto KONDOH, *Residual stress evaluation of railway rails.* JCPDS-International Centre for Diffraction Data, 2009: p. 240-247.
25. Wang, P., et al., *Test Verification and Application of a Longitudinal Temperature Force Testing Method for Long Seamless Rails Using FBG Strain Sensor.* Journal of Sensors, 2016. **2016**: p. 1-11.
26. Yoon, H.-J., et al., *Longitudinal strain monitoring of rail using a distributed fiber sensor based on Brillouin optical correlation domain analysis.* NDT & E International, 2011. **44**(7): p. 637-644.
27. Fateh, M., *Ultrasonic Monitoring of Longitudinal Rail Stress.* US Department of Transportation 2008. **4**.
28. Weaver, R., *Vibration Measurement of Rail Stress* The IDEA Program, Transportation Research Board, National Research Council 2006. **21**: p. 1-15.
29. Verse, *Non-Destructive Stress Free Temperature Measurement.* VORTOK International, 2007. **4**.
30. Aikawa, A., H. Sakai, and K. Abe, *Numerical and Experimental Study on Measuring Method of Rail Axial Stress of Continuous Welded Rails Based on Use of Resonant Frequency.* Quarterly Report of RTRI, 2013. **54**: p. 118-125.
31. Liu Yuxiang, C.X., Jia Xingming, Yi Jin, *Analysis of Plane FEM on Structures of Slab Track in Railway.* Journal of Shijiazhuang Railway Institute, 2006. **19**.

32. Wenlong, T.F.F.S.L., *Eigenvalue Buckling Analysis of The Bearer Frame Based on ANSYS.* JOURNAL OF HEBEI UNIVERSITY OF TECHNOLOGY, 2010. **39**: p. 5.
33. Sinniah Ilanko., L.E.M. and Y. Mochida, *The Rayleigh-Ritz Method for Structural Analysis*. Vol. 229. 2014, UK: ISTE Ltd.
34. Sinniah Ilanko., L.E.M. and Y. Mochida, *The Rayleigh-Ritz Method for Structural Analysis*. Vol. 228. 2014, UK: ISTE Ltd. 11-12.
35. Al Rjoub, Y.S. and A.G. Hamad, *Forced vibration of axially-loaded, multi-cracked Euler-Bernoulli and Timoshenko beams.* Structures, 2020. **25**: p. 370-385.
36. Zhang, X., D. Thompson, and X. Sheng, *Differences between Euler-Bernoulli and Timoshenko beam formulations for calculating the effects of moving loads on a periodically supported beam.* Journal of Sound and Vibration, 2020. **481**.
37. Ghadiri, M. and S.H.S. Hosseini, *Parametric excitation of Euler–Bernoulli nanobeams under thermo-magneto-mechanical loads: Nonlinear vibration and dynamic instability.* Composites Part B: Engineering, 2019. **173**.
38. Nistor, M., R. Wiebe, and I. Stanciulescu, *Relationship between Euler buckling and unstable equilibria of buckled beams.* International Journal of Non-Linear Mechanics, 2017. **95**: p. 151-161.
39. Quy, T.B. and J.-M. Kim, *Crack detection and localization in a fluid pipeline based on acoustic emission signals.* Mechanical Systems and Signal Processing, 2021. **150**.
40. Meserkhani, A., S.M. Jafari, and A. Rahi, *Experimental comparison of acoustic emission sensors in the detection of outer race defect of angular contact ball bearings by artificial neural network.* Measurement, 2021. **168**.
41. Carboni, M. and D. Crivelli, *An acoustic emission based structural health monitoring approach to damage development in solid railway axles.* International Journal of Fatigue, 2020. **139**.
42. Zhang, X., et al., *An improved AE detection method of rail defect based on multi-level ANC with VSS-LMS.* Mechanical Systems and Signal Processing, 2018. **99**: p. 420-433.
43. Zhang, J., et al., *Four distinct anionic heterothiometallic W/S/Ag polymeric clusters directed by solvent-coordinated metal cations.* Polyhedron, 2016. **109**: p. 67-74.
44. Park, J., et al., *Frequency energy shift method for bearing fault prognosis using microphone sensor.* Mechanical Systems and Signal Processing, 2021. **147**.
45. Xiao, K., Q. Wang, and D. Hu, *Post Signal Processing of Ultrasonic Phased Array Inspection Data for Non-destructive Testing.* Procedia Engineering, 2012. **43**: p. 419-424.
46. Zhang, X., et al., *Rail crack detection using acoustic emission technique by joint optimization noise clustering and time window feature detection.* Applied Acoustics, 2020. **160**.

APPENDIX I: Matlab Codes

```
%Critical Load

clear all
n=9;

E = 69.5e9; %(Pa)
I = 9.21E-08; %m^4
L = 1; %m

nm=9;
for i=1:n
    for j=1:n
        if i == j
            K(i,j)=(i*pi)^4;
            M(i,j)=(i*pi)^2;    %K*
        else
            K(i,j)=0;
            M(i,j)=0;
        end
    end
end

[mode,omega]=eig(K,M);
for i=1:n
    P(i)=(omega(i,i));
end
P = sort(P);
P(1)*E*I/L^2
P(2)*E*I/L^2
P(3)*E*I/L^2
P(4)*E*I/L^2
```

```
%Frequency

clear all
n=9;

P=4400    %Given,20% of buckiling load
E = 69.5e9; %(Pa)
I = 9.21E-08; %m^4
L = 1; %m

for i=1:n
      for j=1:n
            if i == j
                  K(i,j)=((i*pi)^4*E*I/L^4)*L/2 ;
                  Ks(i,j)=((i*pi)^2)*L/2 ; %K*
            else
                  K(i,j)=0;
                  Ks(i,j)=0;
            end
      end
end

A=0.9234          %mass per unit length of beam
N=A*L/2         %mass coefficient
M=eye(9)*N      % mass matrix

[mode,omega]=eig(K-P*Ks, M);

for i=1:n
      w(i)=sqrt(omega(i,i));
end

w = sort(w);
w(1)/(2*pi)
w(2)/(2*pi)
w(3)/(2*pi)
w(4)/(2*pi)
```

Appendix II: Spectrogram

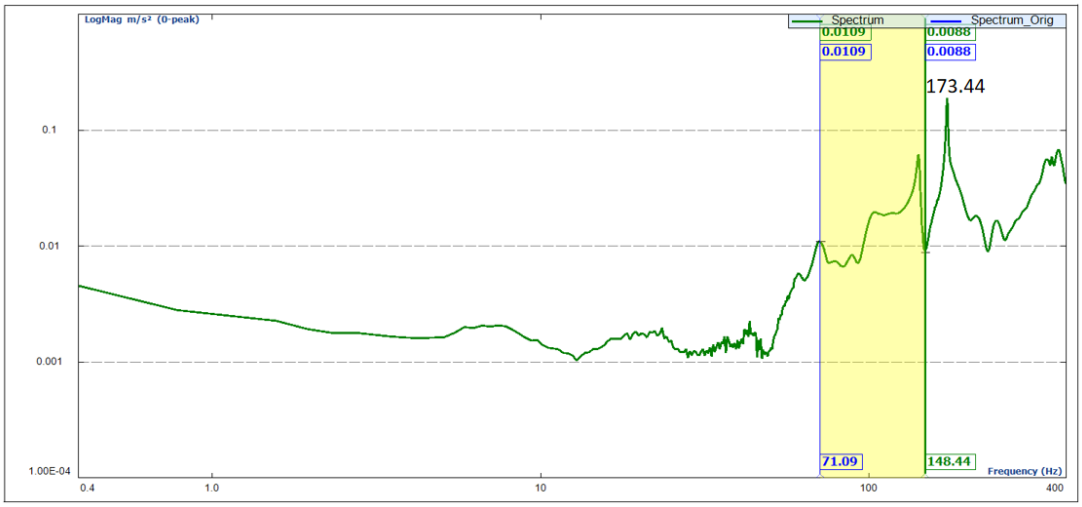

Figure A2.1. The spectrum of the I beam with the accelerometer installed on the right end of the beam, the applied load is 4400N.

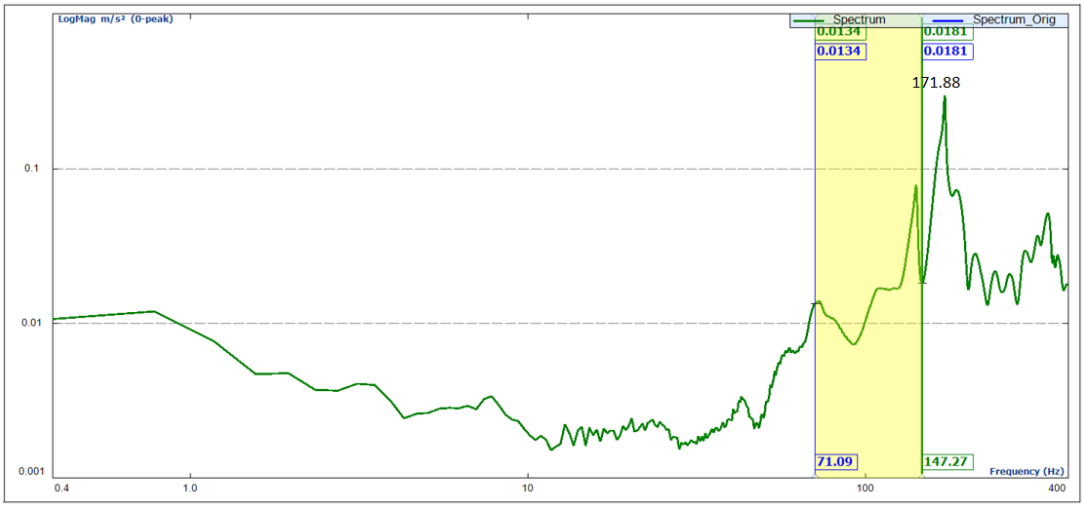

Figure A2.2. The spectrum of the I beam with the accelerometer installed on the center of the beam, the applied load is 4400N.

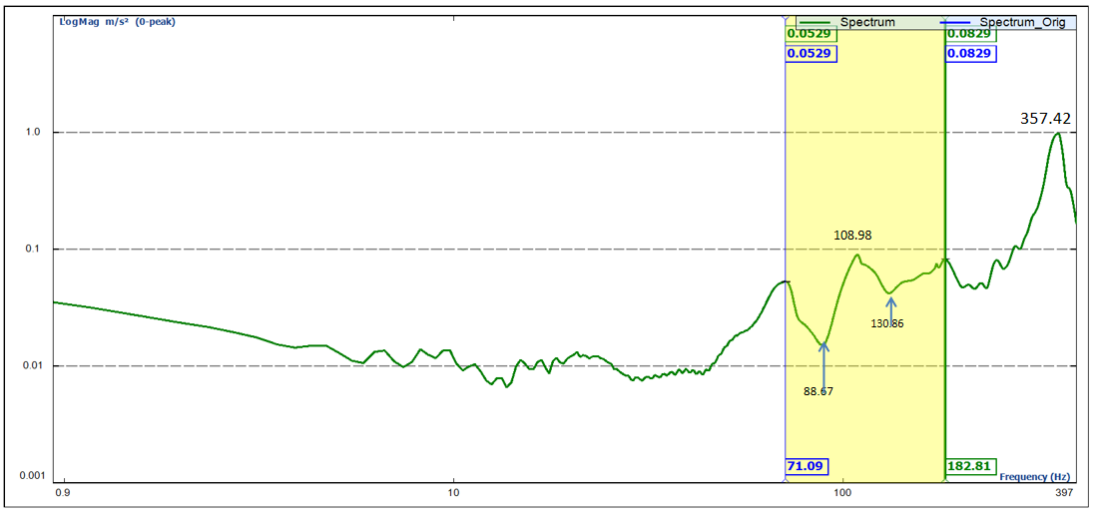

Figure A2.3. The spectrum of the I beam with the accelerometer installed on the right end of the beam, the applied load is 4400N.

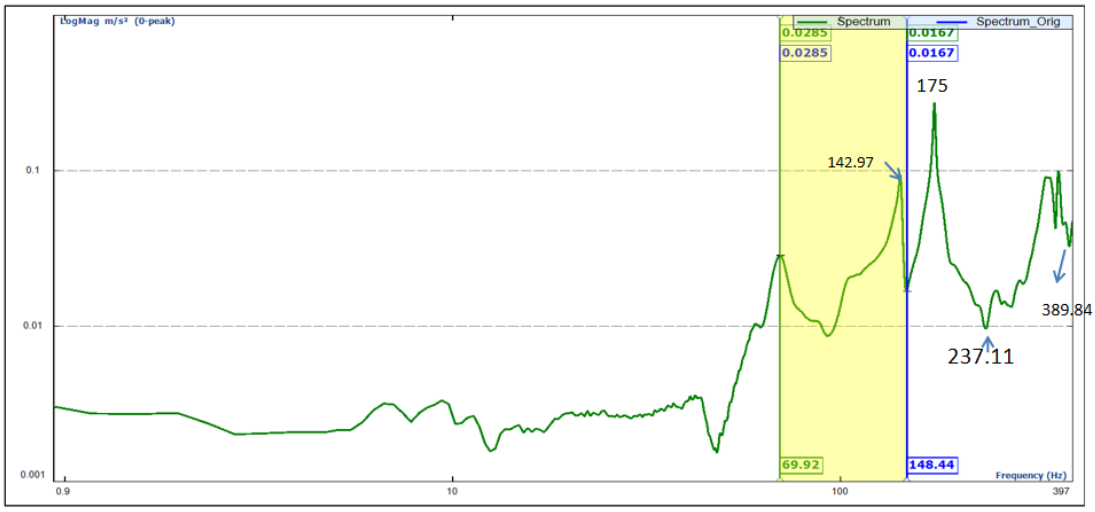

Figure A2.4. The spectrum of the I beam with the accelerometer installed on the left end of the beam, the applied load is 8800N.

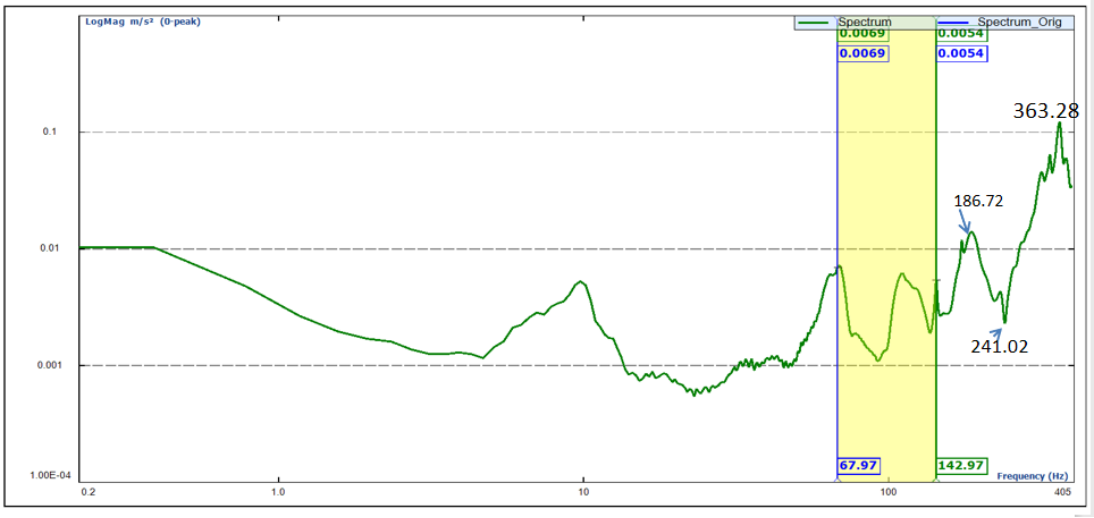

Figure A2.5. The spectrum of the I beam with the accelerometer installed on the center of the beam, the applied load is 8800N.

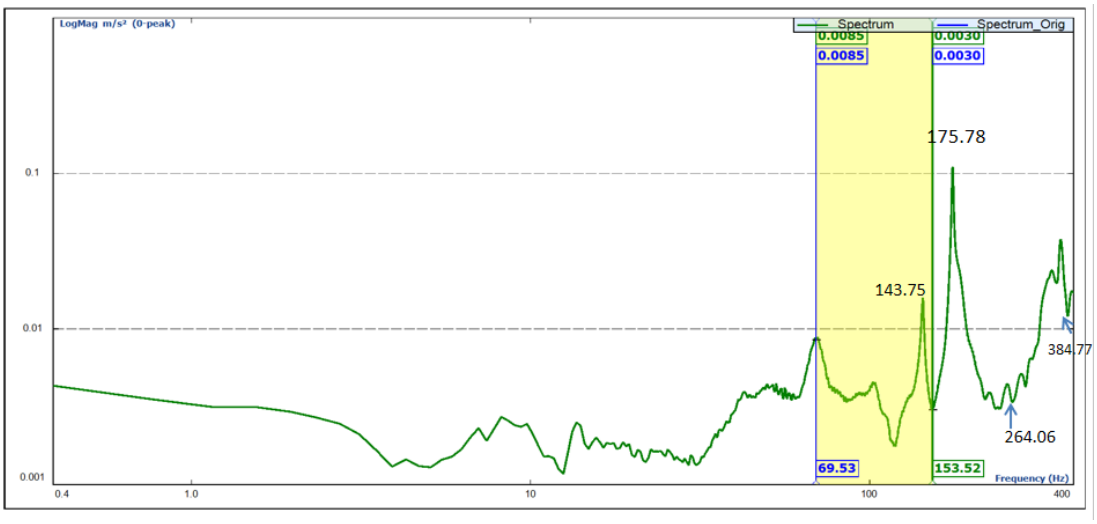

Figure A2.6. The spectrum of the I beam with the accelerometer installed on the right end of the beam, the applied load is 8800N.

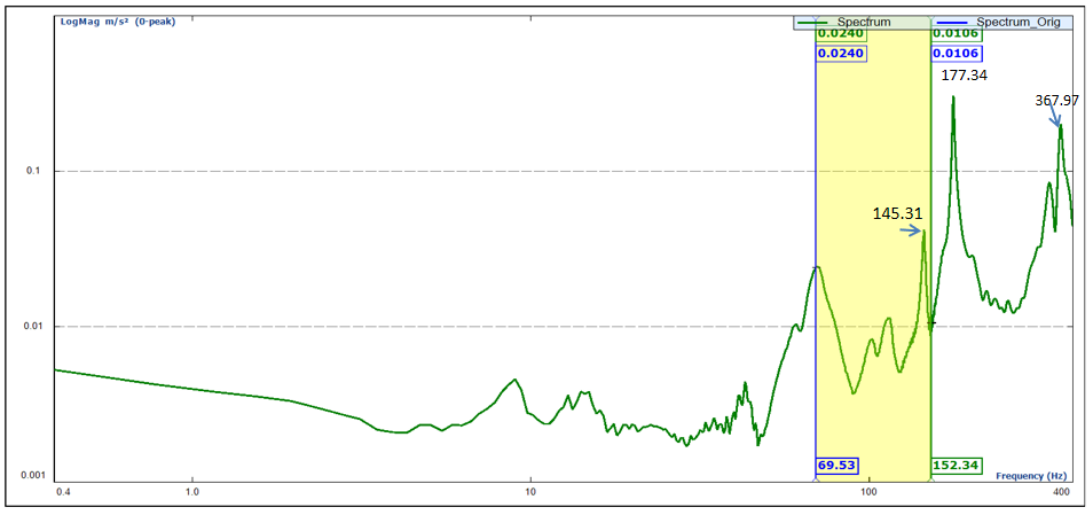

Figure A2.7. The spectrum of the I beam with the accelerometer installed on the left end of the beam, the applied load is 13201N.

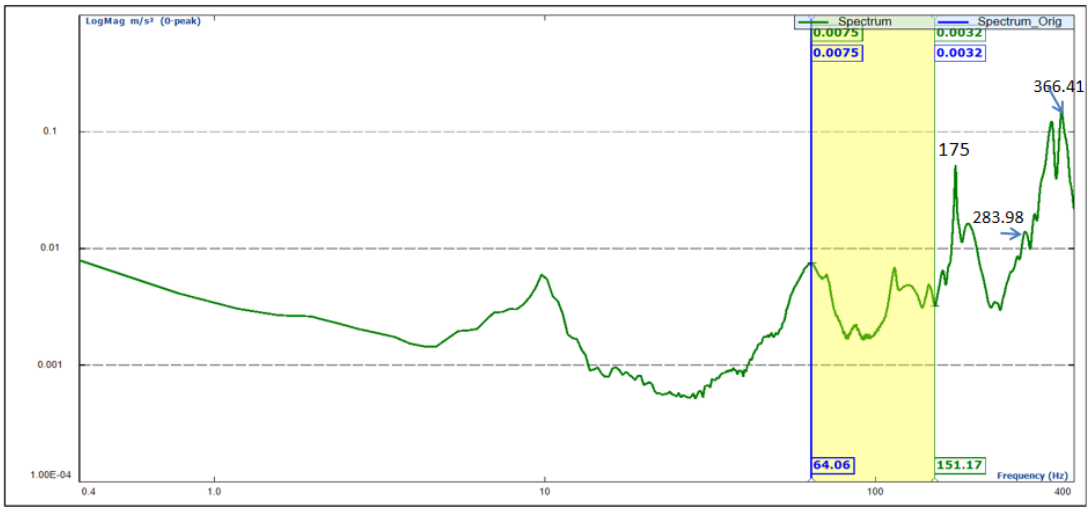

Figure A2.8. The spectrum of the I beam with the accelerometer installed on the center of the beam, the applied load is 13201N.

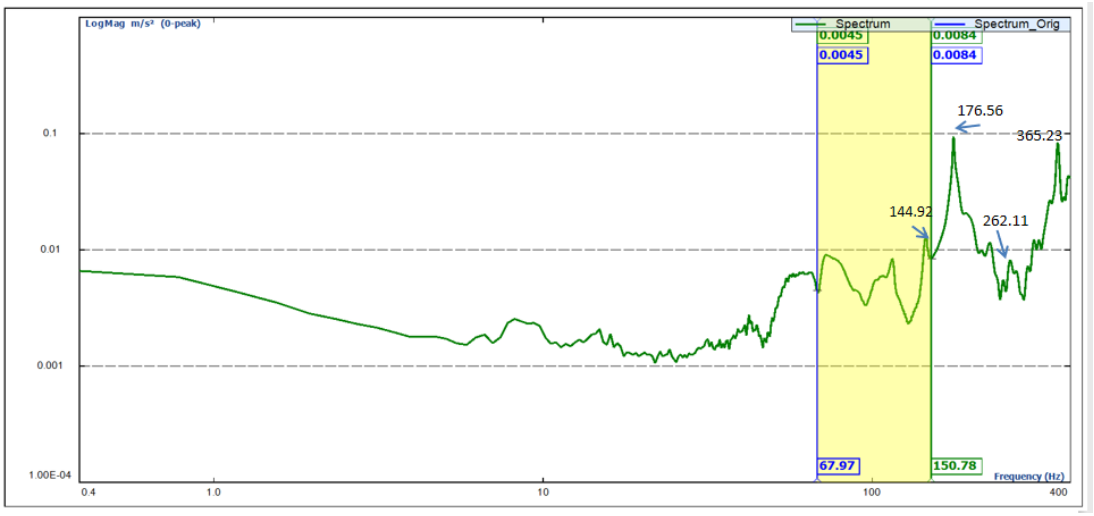

Figure A2.9. The spectrum of the I beam with the accelerometer installed on the right end of the beam, the applied load is 13201N.

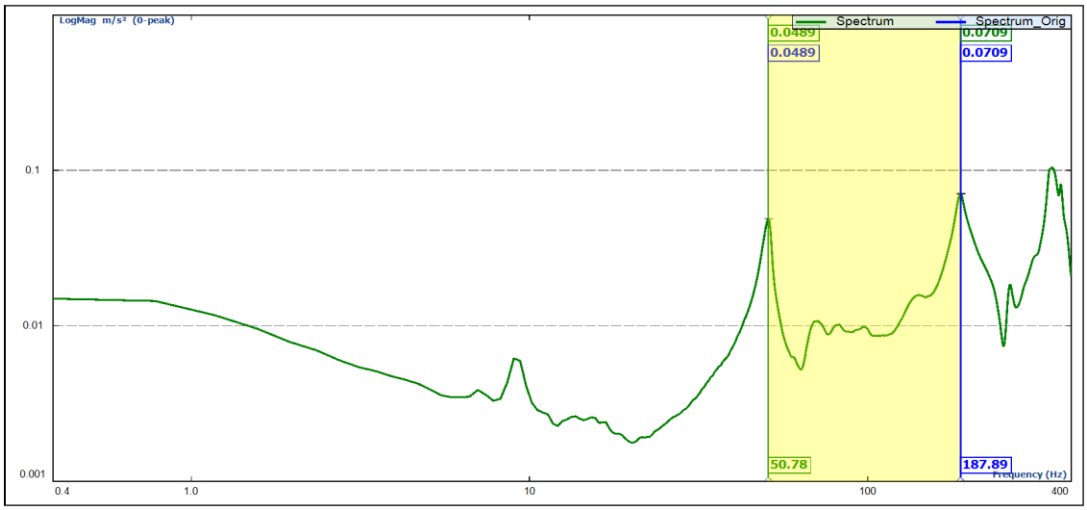

Figure A2.10. The spectrum of the T beam with the accelerometer installed on the left end of the beam, the applied load is 773N.

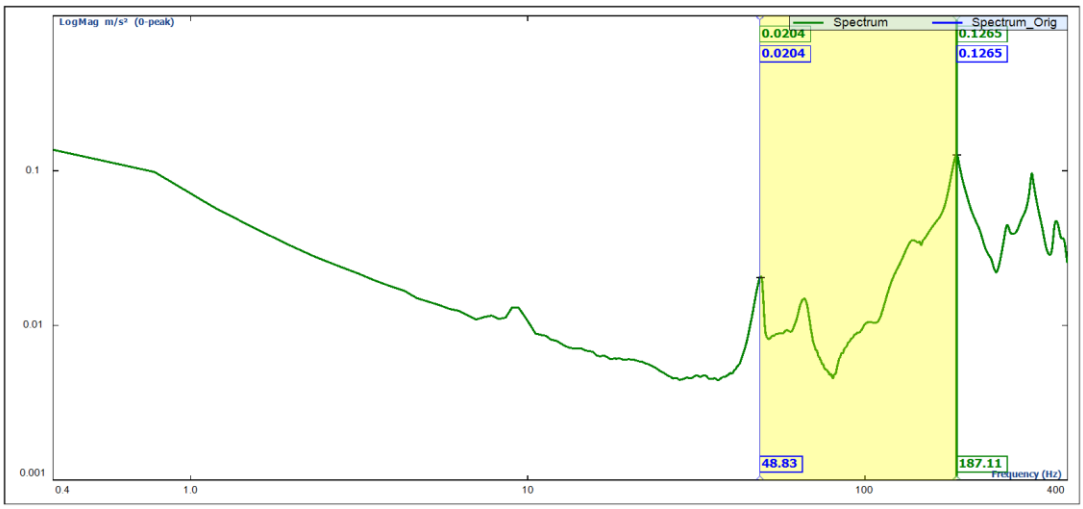

Figure A2.11. The spectrum of the T beam with the accelerometer installed on the center of the beam, the applied load is 773N.

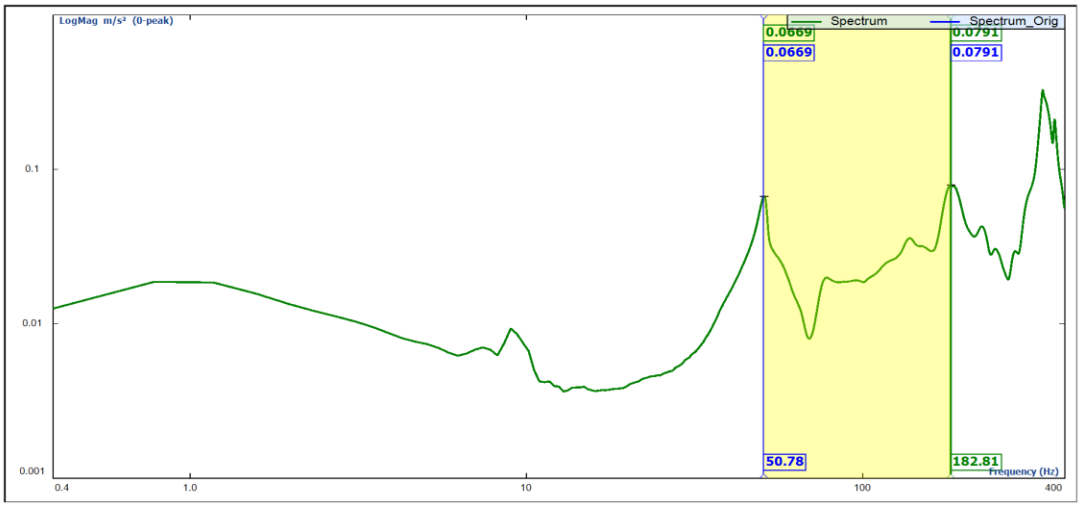

Figure A2.12. The spectrum of the T beam with the accelerometer installed on the right end of the beam, the applied load is 773N.

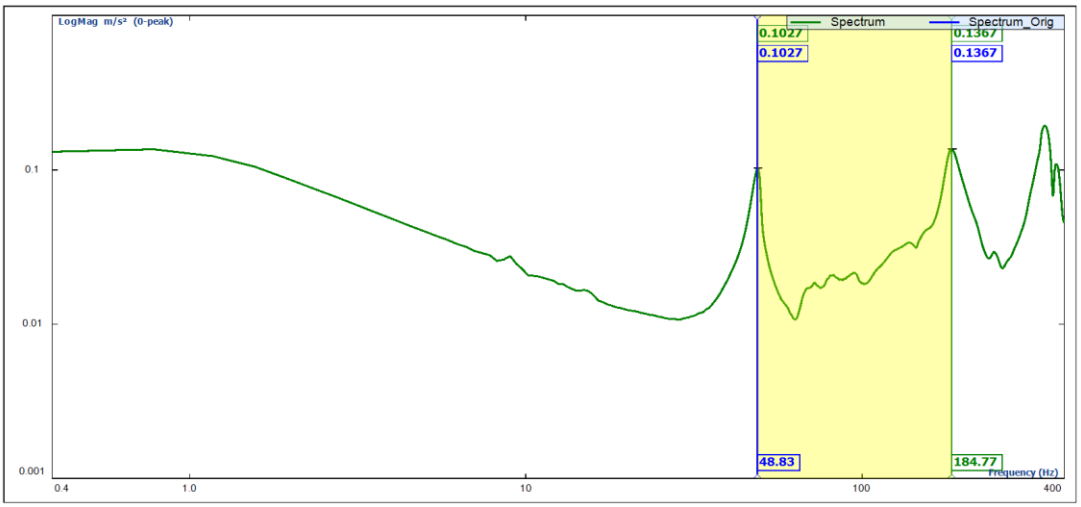

Figure A2.13. The spectrum of the T beam with the accelerometer installed on the left end of the beam, the applied load is 1154.67N.

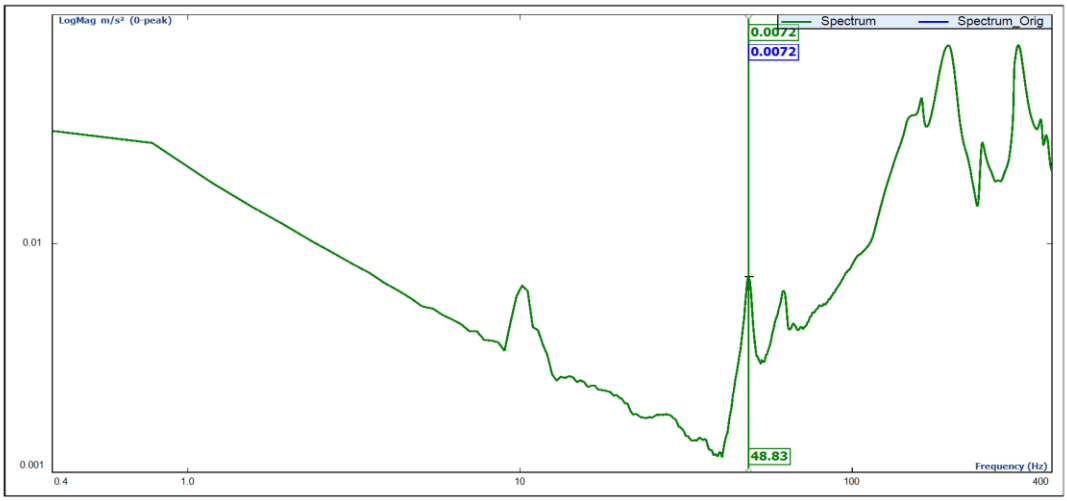

Figure A2.14. The spectrum of the T beam with the accelerometer installed on the center of the beam, the applied load is 1154.67N.

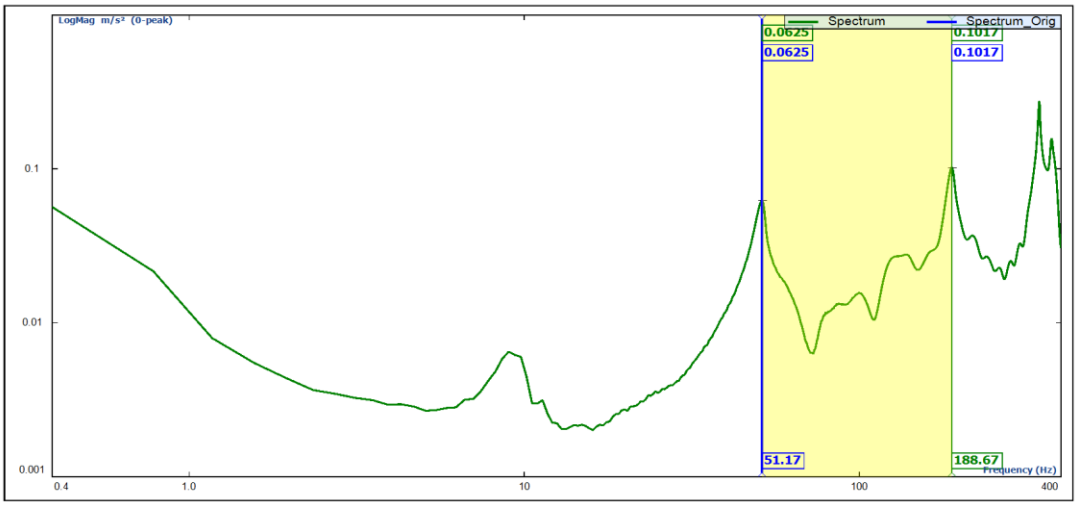

Figure A2.15. The spectrum of the T beam with the accelerometer installed on the right of the beam, the applied load is 1154.67N.

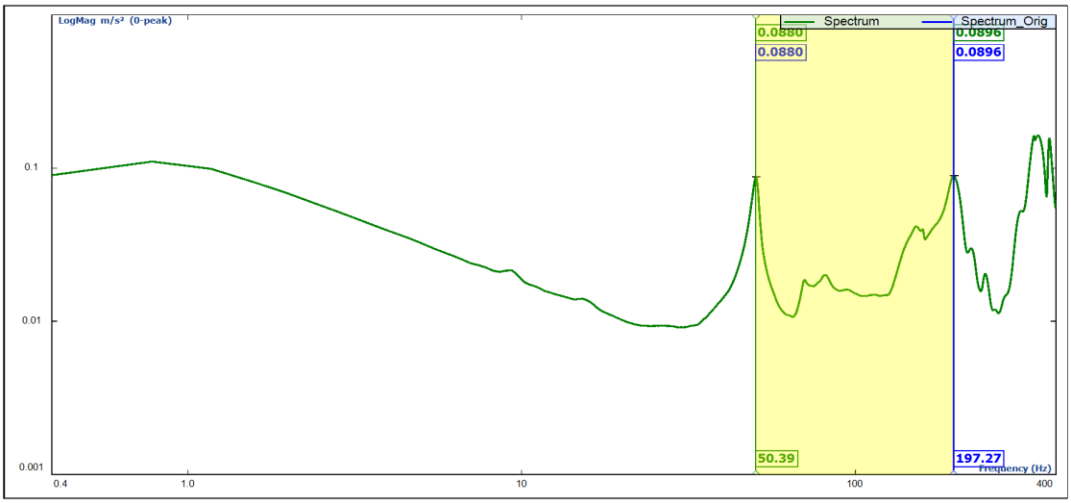

Figure A2.16. The spectrum of the T beam with the accelerometer installed on the left end of the beam, the applied load is 1450.7N.

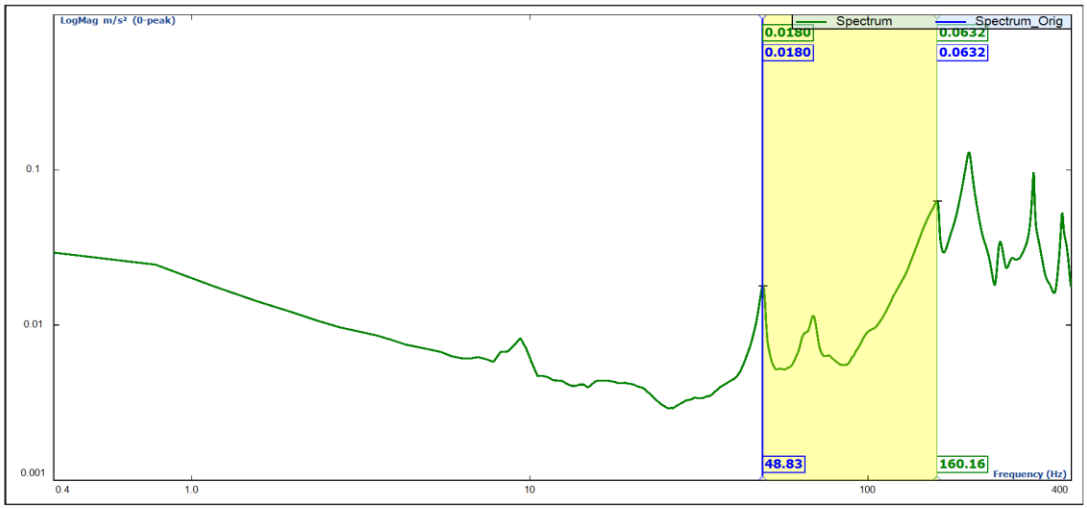

Figure A2.17. The spectrum of the T beam with the accelerometer installed on the center of the beam, the applied load is 1450.7N.

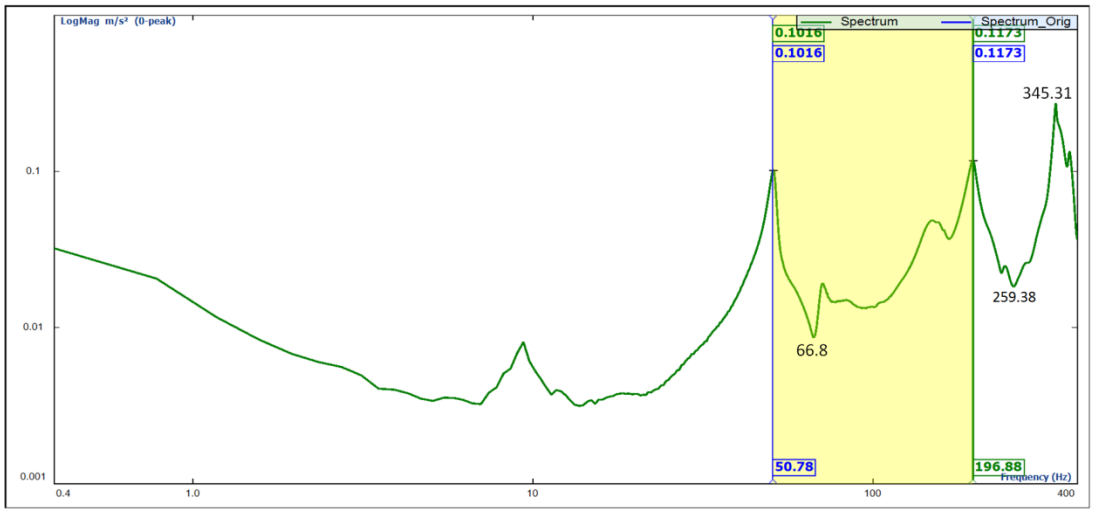

Figure A2.18. The spectrum of the T beam with the accelerometer installed on the right end of the beam, the applied load is 1450.7N.

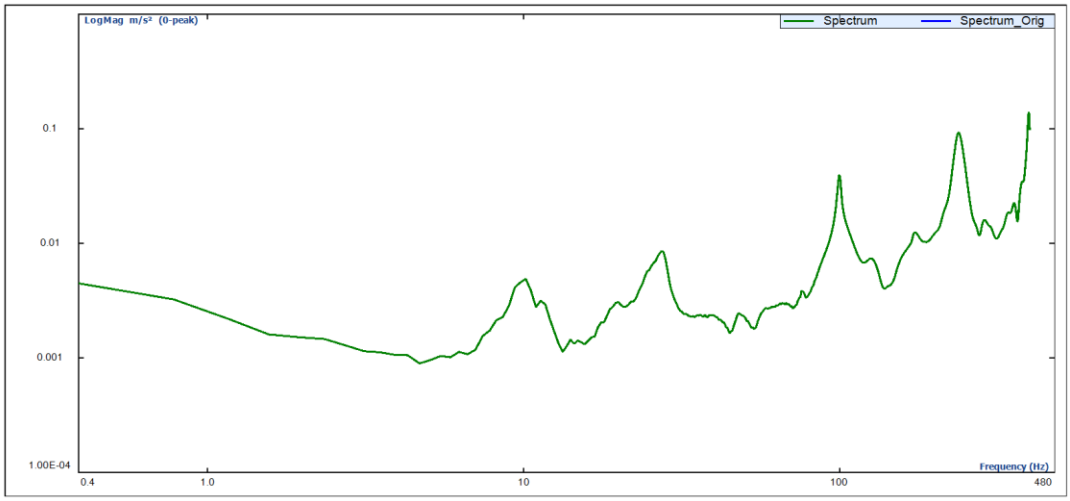

Figure A2.19. The spectrum of the steel beam with the accelerometer installed on the left end of the beam, the applied load is 847N.

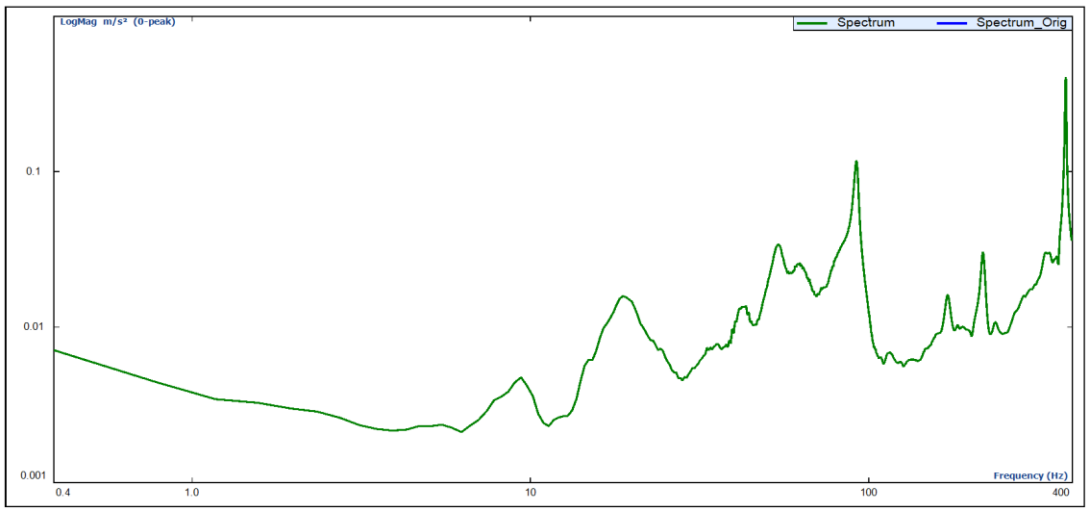

Figure A2.20. The spectrum of the steel beam with the accelerometer installed on the center of the beam, the applied load is 847N.

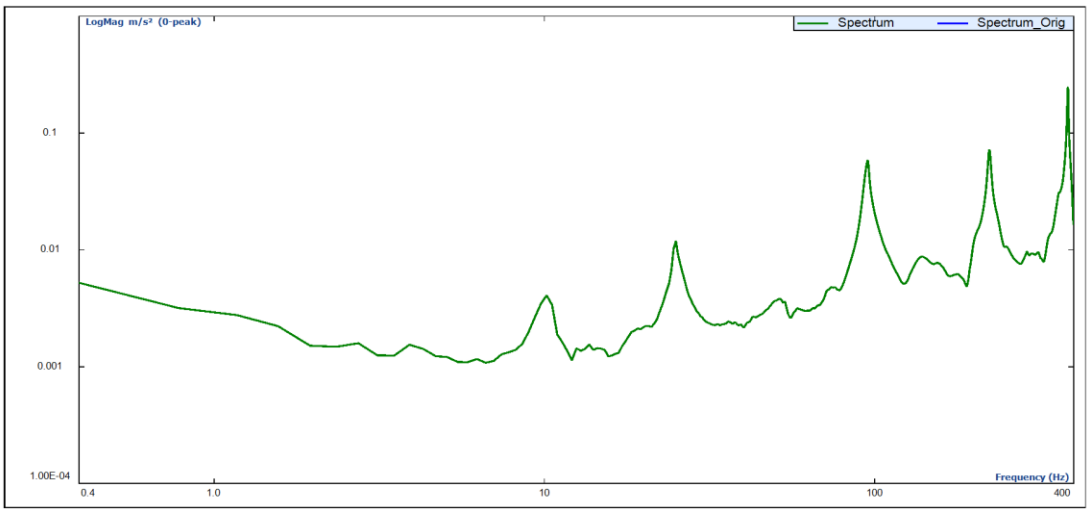

Figure A2.21. The spectrum of the steel beam with the accelerometer installed on the right end of the beam, the applied load is 847N.

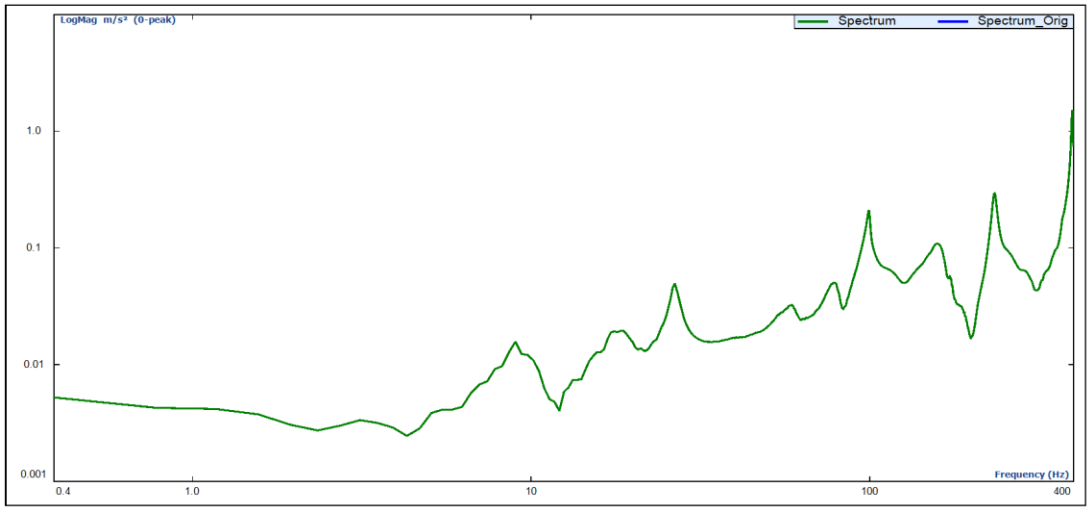

Figure A2.22. The spectrum of the steel beam with the accelerometer installed on the left end of the beam, the applied load is 1694N.

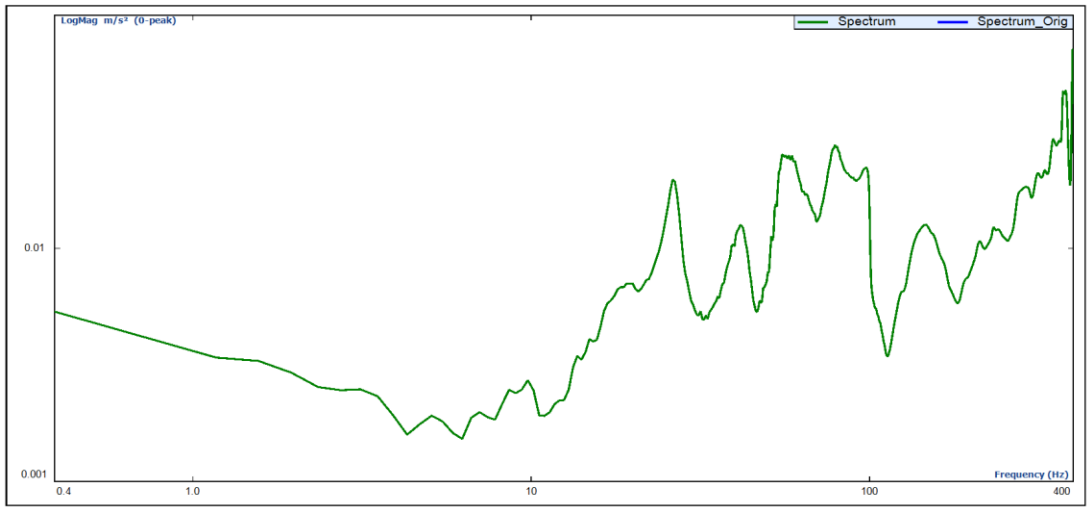

Figure A2.23. The spectrum of the steel beam with the accelerometer installed on the center of the beam, the applied load is 1694N.

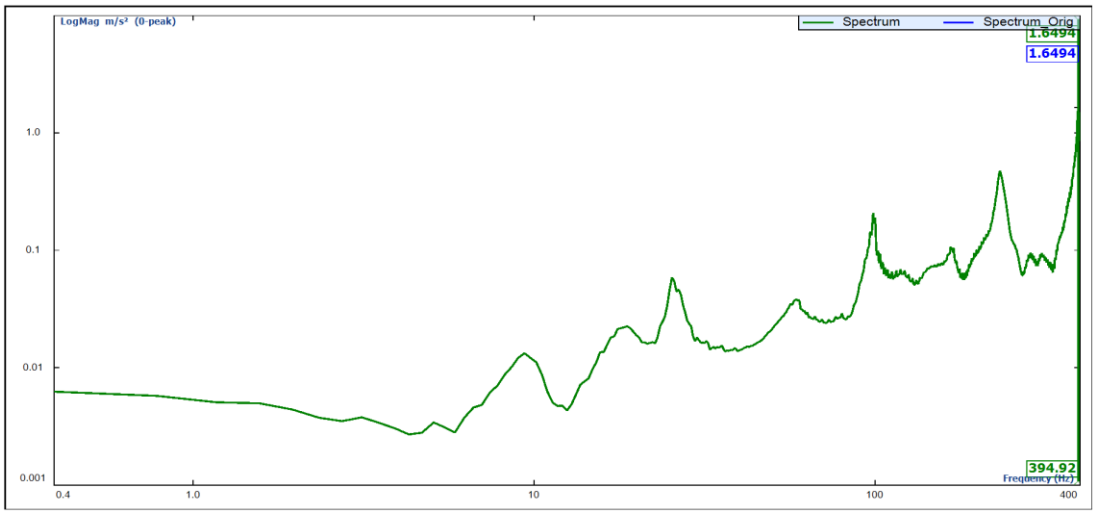

Figure A2.24. The spectrum of the steel beam with the accelerometer installed on the right end of the beam, the applied load is 1694N.

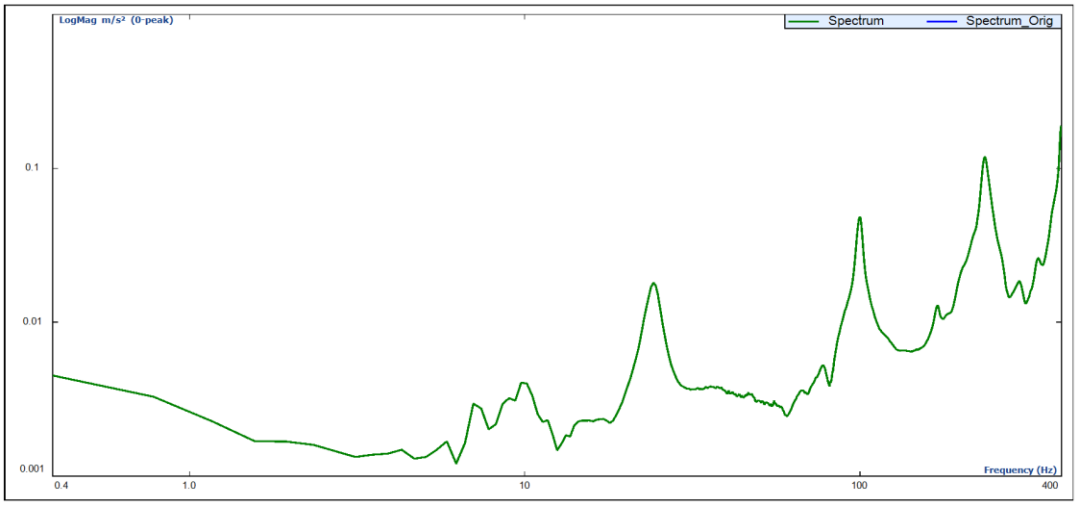

Figure A2.25. The spectrum of the steel beam with the accelerometer installed on the left end of the beam, the applied load is 2541N.

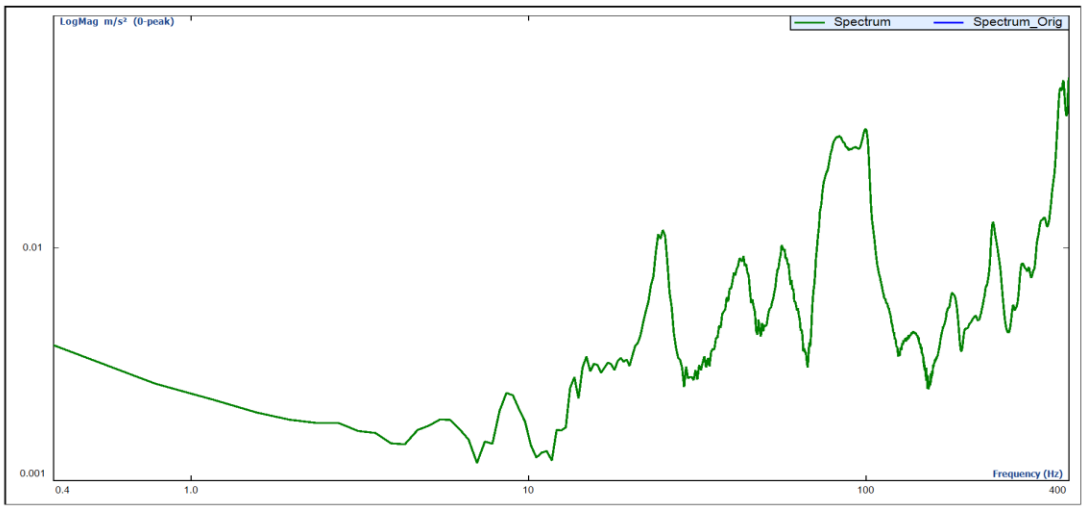

Figure A2.26. The spectrum of the steel beam with the accelerometer installed on the center of the beam, the applied load is 2541N.

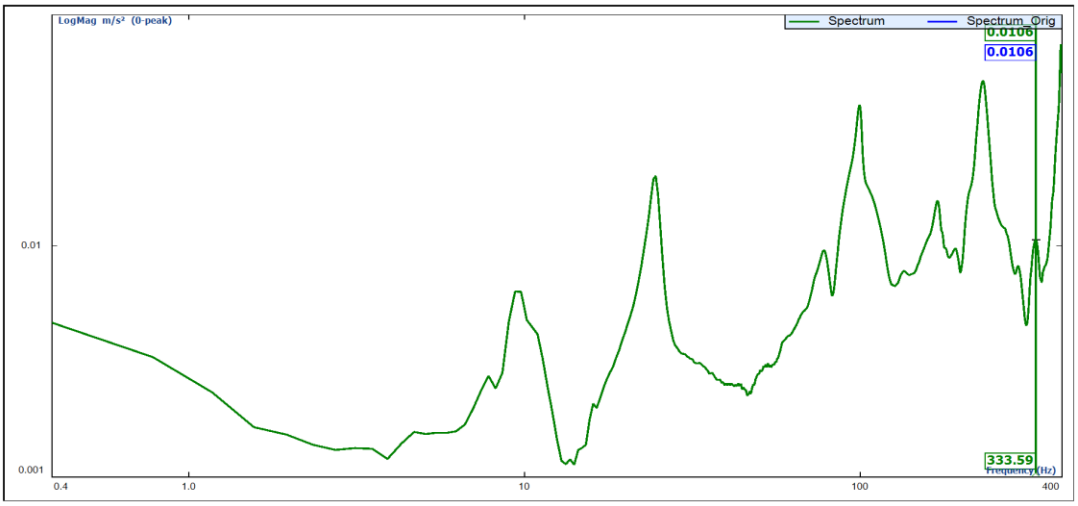

Figure A2.27. The spectrum of the steel beam with the accelerometer installed on the right end of the beam, the applied load is 2541N.

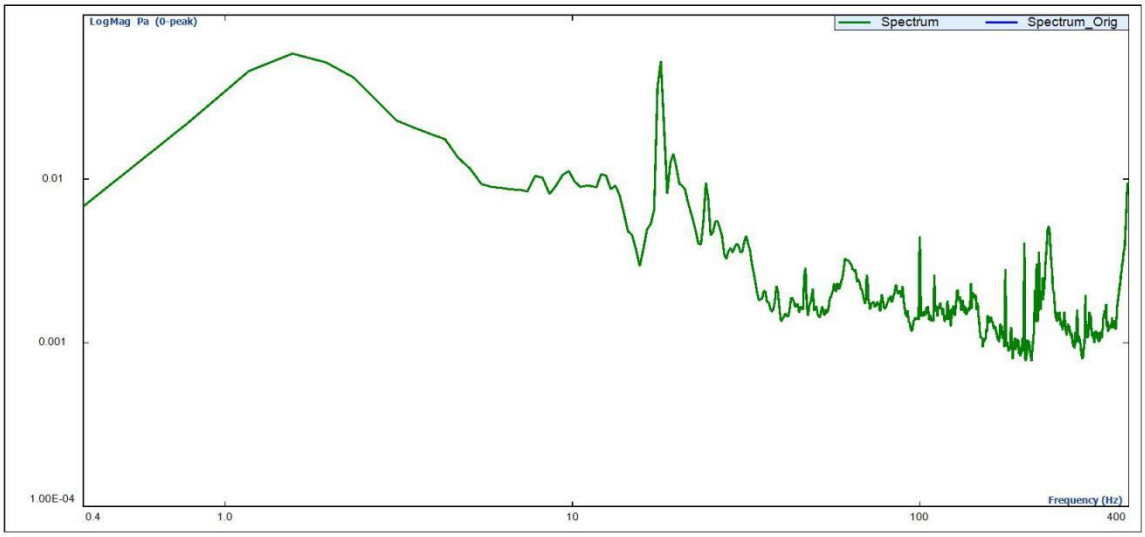

Figure A2.28. The spectrum of the steel beam with the microphone, the applied load is 847N.

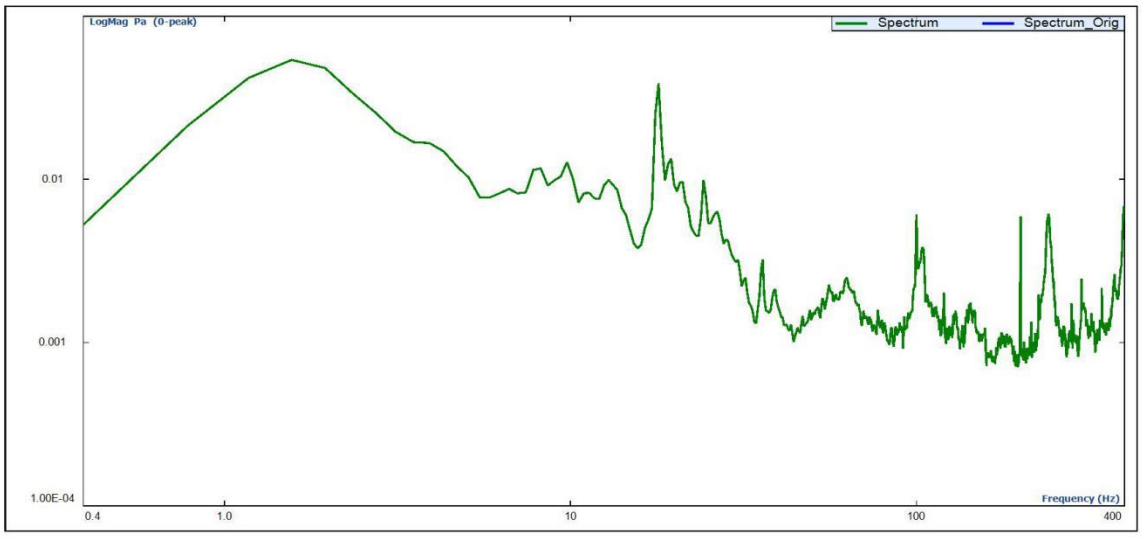

Figure A2.29. The spectrum of the steel beam with the microphone, the applied load is 1694N.

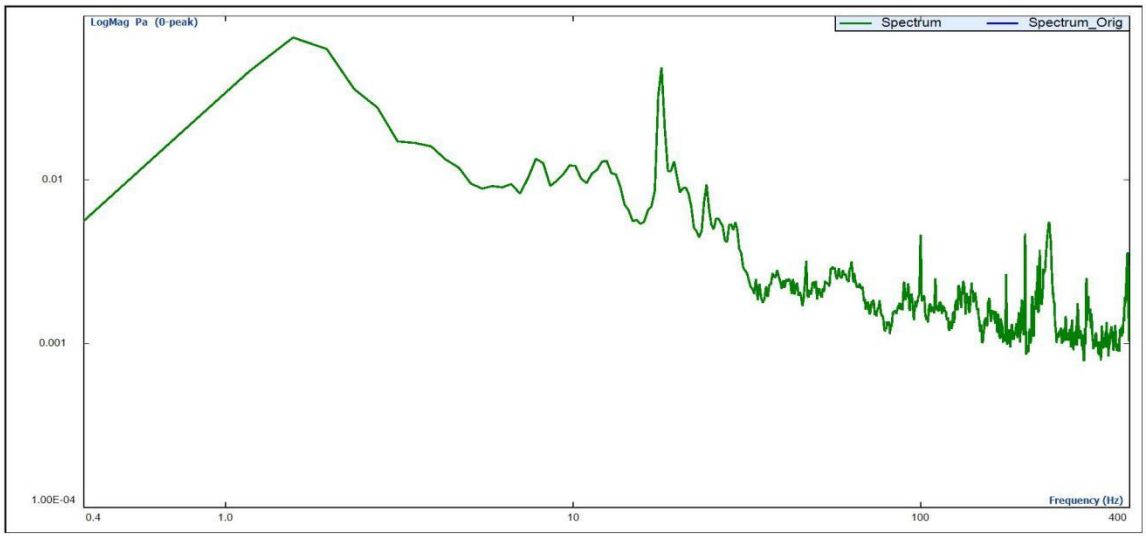

Figure A2.30. The spectrum of the steel beam with the microphone, the applied load is 2541N.

Appendix III: The Values of strain gauge

The strain gauge records the strain value applied to beams during the experiment. The relationship between strain and axial force is as follows:

$$\sigma = \varepsilon E = P/A \tag{A3.1}$$

$$P = \varepsilon E A \tag{A3.2}$$

E is the Young's modulus, σ is the stress in the beam, ε is the strain in the beam, A is the cross section of the beam, and P is the axial force. According to Eq. A3.2, the axial force can be converted from the corresponding strain value. The strain values measured in each beam are shown in Table A3.1-A3.3.

Table A3.1. The strain values applied to the I beam during the experiment.

I Beam			
strain (με)			
Position	CH 1	CH 2	CH3
1	191	200	205
2	208	205	190
3	179	192	197
1	347	368	375
2	372	395	403
3	351	373	382
1	517	547	560
2	540	570	584
3	500	528	541

Table A3.2. The strain values applied to the T beam during the experiment.

T Beam			
strain (με)			
Position	CH 1	CH 2	CH3
1	51	80	99
2	51	78	93
3	51	77	93
1	88	125	141
2	79	111	133
3	85	117	136
1	59	152	232
2	55	146	237
3	54	143	236

Table A3.3. The strain values applied to the steel beam during the experiment.

Steel Beam			
strain (με)			
Position	CH 1	CH 2	CH3
1	36	19	13
2	57	18	19
3	59	17	19
1	106	34	71
2	96	35	64
3	117	37	89
1	115	58	30
2	131	61	30
3	126	58	31